INL/RPT-24-76428
Revision 000

Heat Pipe Cooled Microreactors

January 2024

Ilyas Yilgor, Zachary D. Sellers, Jeremy L. Hartvigsen, Piyush Sabharwall
Idaho National Laboratory

Katrina M. Sweetland
Los Alamos National Laboratory

INL is a U.S. Department of Energy National Laboratory operated by Battelle Energy Alliance, LLC

INL/RPT-24-76428

Heat Pipe Cooled Microreactors

Ilyas Yilgor, Zachary D. Sellers, Jeremy L. Hartvigsen, Piyush Sabharwall
Idaho National Laboratory

Katrina M. Sweetland
Los Alamos National Laboratory

January 2024

Idaho National Laboratory
Idaho Falls, Idaho 83415

http://www.inl.gov

Prepared for the
U.S. Department of Energy
Office of Nuclear Energy
Under DOE Idaho Operations Office
Contract DE-AC07-05ID14517

ABSTRACT

Microreactor technologies are required to provide reliable carbon-free power generation in remote applications. The heat pipe cooled microreactor concept in particular offers notable advantages due to the passive operation of heat pipes enabling increased reliability and simplicity in a more compact form factor. There is a significant need for experimental work to aid and expedite the deployment of heat pipe microreactors due to their unique technological characteristics. Thus, there has been increased interest in heat pipe experiments by numerous institutions in order to support these efforts. The present work is a comprehensive review of heat pipe experiments, describing instrumentation, methods, phenomena of interest, and recent developments. In addition, legacy work on the operation of high-temperature heat pipes under irradiation is reviewed and discussed. Furthermore, the verification and validation efforts for the flagship heat pipe simulation code, Sockeye, are reviewed and requirements for future experiments are outlined. Finally, future directions are proposed for heat pipe experimentation.

Page intentionally left blank

ACKNOWLEDGEMENTS

This work was supported by the U.S. Department of Energy–Office of Nuclear Energy (DOE-NE) under the Idaho National Laboratory (INL) Advanced Reactor Technology (ART) portfolio's Microreactor Program (MRP).

The authors extend their thanks to researchers from the highlighted institutions for their support. They specifically acknowledge Pei-Hsun Huang, Taehwan Ahn, Annalisa Manera, and Victor Petrov of the University of Michigan (UM) for their contributions to Section 4.5, both in writing and reviewing.

Subsequent thanks go to Joseph Seo and Yassin Hassan of Texas A&M University (TAMU) for their reviewing and editing of Section 4.4, Mark Anderson of the University of Wisconsin–Madison (UW–Madison) for his reviewing and editing of Section 4.6, and Joshua Hansel of INL for his review of Section 6.

Last, the authors acknowledge Robert S. Reid of Los Alamos National Laboratory (LANL) and Shanbin Shi of Rensselaer Polytechnic Institute (RPI) for their overall guidance and technical support.

Page intentionally left blank

CONTENTS

FIGURES

TABLES

ACRONYMS

ACT	Advanced Cooling Technologies
B_4O	boron carbide
BeO	beryllium oxide
CAD	computer-aided drawing
CT	computerized tomography
DC	direct current
DIC	digital image correlation
DOE	U.S. Department of Energy
DTS	distributed temperature sensor
EBR-II	Experimental Breeder Reactor II
FBG	fiber Bragg grating
FO-DTS	fiber-optic distributed temperature sensor
HEDL	Hanford Engineering Development Laboratory
HEU	highly-enriched uranium
HPMR	Heat Pipe MicroReactor
HTC	heat transfer coefficient
INL	Idaho National Laboratory
IR	infrared
KRUSTY	Kilowatt Reactor Using Stirling TechnologY
LANL	Los Alamos National Laboratory
LTHPF	Low-Temperature Heat Pipe Test Facility
LWR	light water reactor
MAGNET	Microreactor Agile Non-nuclear Experimental Test
MISOH	Michigan Sodium Heat Pipe Facility
MOOSE	Multiphysics Object Oriented Simulation Environment
$MoSi_2$	molybdenum disilicide
MRP	Microreactor Program
NASA	National Aeronautics and Space Administration
NEAMS	Nuclear Energy Advanced Modeling and Simulation
NEUP	Nuclear Energy University Programs
NRL	Naval Research Laboratory
NNSA	National Nuclear Security Administration
NNSS	Nevada National Security Site

NRC	U.S. Nuclear Regulatory Commission
ODFR	optical frequency domain reflectometry
ORNL	Oak Ridge National Laboratory
OWR	Omega West Reactor
PCS	power conversion system
PID	proportional-integral-derivative
PIE	post-irradiation examination
PTFE	polytetrafluoroethylene
R&D	research and development
RPI	Rensselaer Polytechnic Institute
SCR	silicon controlled rectifier
SPHERE	Single Primary Heat Extraction and Removal Emulator
SPR	Special Purpose Reactor
TAMU	Texas A&M University
TC	thermocouple
TIG	tungsten inert gas
U.S.	United States
UM	University of Michigan
UT	ultrasonic thermometer
UW–Madison	University of Wisconsin–Madison
WEC	Westinghouse Electric Company

HEAT PIPE COOLED MICRORECTORS

1. INTRODUCTION

Microreactors are crucial in satisfying the need for compact, portable, and safe carbon-free power generation in applications ranging from disaster relief, remote military operations, space power, and backup power [1]. They are characterized by their compact form factor, rapid deployment capabilities, and low-power outputs in the kilowatt (kW) to lower megawatt (MW) range. Microreactors are expected to be initially utilized in remote or off-the-grid locations [2]. A recent study by Aumeier et al. on markets for microreactors in the United States (U.S.) specified potential markets—specifically in the states of Alaska and Wyoming [3], two of the most scarcely populated states in the country—where compact or mobile microreactors could provide great utility in civic, commercial, and defense applications. The identified commercial opportunities included niche markets with high-energy costs, energy-intensive industries, value-added materials manufacturing, process heat generation, and decarbonization policy-driven markets. Applications in these markets include mining operations, seafood processing plants, deep water ports, and data centers. Separate economic analyses identified cost drivers [4], and showed that microreactors are cost-competitive with systems of similar size, such as diesel generators and renewable sources in microgrids [5].

Among other small modular reactors and microreactors, the Heat Pipe MicroReactor (HPMR) concept in particular offers unique advantages compared to conventional light water reactors (LWRs) [6] and other advanced reactor designs by utilizing heat pipes with alkali metal working fluids to harvest the heat generated in the reactor core. Heat pipes can be classified as high-efficiency passive two-phase heat transfer devices that operate through the cyclic evaporation and condensation of a working fluid [7]. A schematic describing the operating principle of heat pipes can be seen in Figure 1, where the working fluid evaporates in an evaporator and later flows to a condenser, where the fluid condenses and returns to the evaporator via the aid of a wick structure and/or gravity. These designs have a diverse range of applications that include nuclear microreactors [8, 9], electronics [10], solar thermal plants [11, 12], furnaces [13], heat exchangers [14], and turbines [15]. The advantages of HPMRs mainly arise from their compact size, the passive operation of the heat pipes, and the elimination of intricate coolant pumping systems, which also enables increased reliability.

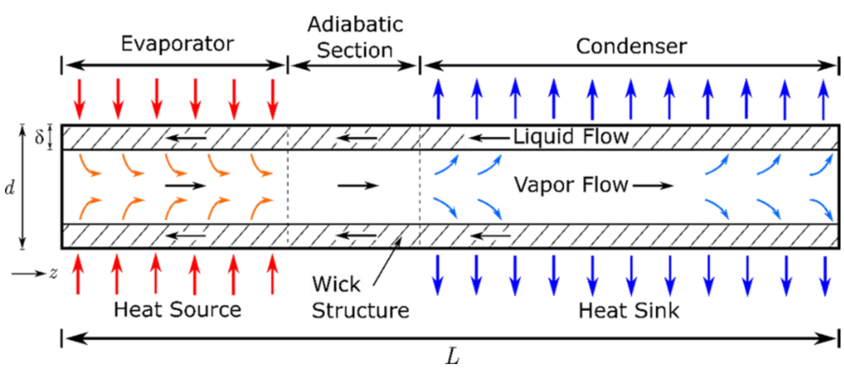

Figure 1. A schematic describing heat pipe operation [16].

Numerous governmental, commercial, and academic institutions from multiple countries aid the deployment of HPMRs. In particular, HPMR development for civilian applications is being spearheaded by the U.S. Department of Energy (DOE) Microreactor Program (MRP) [1, 17-21], which involves several DOE national laboratories, as well as academic and commercial partners, and builds on the work that was initiated at Los Alamos National Laboratory (LANL) in the twentieth century [22-26]. On the commercial side, the eVinci™ Microreactor is under development by Westinghouse Electric Company (WEC) [27, 28].

The research and development (R&D) efforts for HPMRs include a variety of studies using analytical, numerical, and experimental methods [14, 29-32]. In particular, there has been a recent acceleration in experimental work related to heat pipes for microreactor applications, because detailed high-fidelity experimental data is lacking in literature. Experimental work is needed to support technology maturation and demonstration efforts, which are designated as focus areas by the MRP [17]. Furthermore, a comprehensive experimental database: (1) can allow a better understanding of heat pipe operation including transients and accident scenarios, (2) be utilized for the verification and validation of models used in heat pipe and reactor design, (3) enhance the performance and reliability of wick structures through novel designs and fabrication techniques, and (4) enable the establishment of regulatory requirements. Therefore, experiments utilizing state-of-the-art methods and instrumentation are a necessary step on the path to HPMR deployment.

The present work is structured as follows: Section 2 provides a background on different heat pipe experimental methods and approaches, Section 3 identifies phenomena of interest in heat pipes, Section 4 reviews recent heat pipe experimental work conducted in leading U.S. institutions, Section 5 reviews legacy work on the operation of heat pipes under irradiation, Section 6 analyzes verification and validation efforts of the Sockeye heat pipe code, Section 7 presents a summary of recent experiments and proposes future directions, and Section 8 provides some concluding remarks.

2. BACKGROUND ON HEAT PIPE EXPERIMENTS

Experiments usually focus on various aspects of heat pipe operation, such as the investigation of operating limits [33-38], wick development and performance [39], working fluid fill ratio [35, 40-42], start-up transients [43, 44], inclination angles [41, 45, 46], novel instrumentation [16, 43, 47], two-phase flow characteristics [48], and motion conditions [49]. This subsection discusses some of these different experimental approaches.

2.1 Operating Limits

Conventional heat pipe analysis considers multiple limits that include the viscous, sonic, entrainment, capillary, and boiling limits. These limits and others are described in detail in the classical texts by Faghri [7], Dunn and Reay [50], and Chi [51]. The viscous limit occurs at relatively low operating temperatures where the vapor pressure in the evaporator is not sufficient to drive the vapor flow toward the condenser section. The sonic limit is due to choking in the vapor flow limiting the mass flow rate. The capillary limit is characterized by the capillary pressure not being sufficient to balance the pressure drops along the heat pipe. Entrainment limit is reached when the vapor flow shears off the liquid at high-velocities, causing the wick to dry out. The boiling limit is due to boiling, which causes the wick structure to dry out and block the liquid flow along the wick. The limit for a particular case depends on the heat pipe geometry, wick structure, working fluid, and operating conditions. For instance, viscous and sonic limits are significant at lower heat pipe operating temperatures, as opposed to the boiling limit, which is significant at much higher temperatures especially for liquid-metal working fluids. Although the performance of a heat pipe must be characterized holistically based on the particular application, the concept of operating limits provides a practical means of evaluating heat pipe performance. Therefore, many existing works in literature have focused on the experimental evaluation of operating limits and the development of limit models [7, 37, 51].

Due to the different physical phenomena that are in effect for the different operating limits, indirect methods must often be used to determine which limit is reached. The operating limits are usually characterized by an abrupt increase in the overall thermal resistance of the heat pipe, which effectively results in higher temperatures [24, 35]. Thus, the power at which the limit is reached can usually be determined based on the temperature measurements. Analytical estimates and physics-based reasoning can then be employed to determine the limiting factor based on the experimental context and the evaporator exit temperature, which is conventionally used in the definition of operating limits. However, it should be noted that operating limits can change both in the short-term during transients and the long-term due to effects such as corrosion and the introduction of non-condensable gasses.

2.2 Wick Investigations

A well-designed wick structure is a crucial component of a heat pipe that has a great influence on its overall performance since it is imperative in enabling liquid return to the evaporator in most heat pipe designs. Therefore, many researchers have previously investigated the performance and fabrication methods of both conventional and novel wick designs [39, 52-54]. In general, the type of wick structure must be chosen specifically based on the application. For instance, HPMR applications typically utilize heat pipes with high length-to-diameter ratios [2, 8]; this dictates the use of wicks with relatively high permeabilities rather than capillary pumping abilities in order to achieve high capillary limits. This is due to the parameters' competing effects in enabling low flow resistance versus increased capillary pressure. The annulus-screen wick is commonly used for such applications as it provides a low resistance flow path to the liquid [54]. In addition, efforts exist on the utilization of additive manufacturing technologies for heat pipe and wick fabrication [55-57]. This technology enables the free-form production of heat pipe wick structures and the tailoring of wick properties such as pore size and permeability [58].

Investigations of novel wick designs or manufacturing techniques usually involve the characterization of wick properties that are significant for heat transfer applications. These properties may include the permeability, effective pore radius, effective thermal conductivity, porosity, wettability, and surface morphology [59, 60]. Most properties can be measured utilizing an array of methods and instruments, ranging from test rigs utilizing simple physical phenomena to cutting-edge equipment [56, 61]. After a wick is characterized, its performance in heat pipe applications can be estimated based on the measured parameters. Later, the wick's performance during operation can be examined within a heat pipe and the wick properties can be used in model development or validation.

2.3 Steady-State and Transients

Operating limits and wick investigations described in the preceding sections are usually characterized by steady-state experiments. However, it is particularly important in nuclear applications to understand and predict start-up, shut-down, and power transients, as well as accident scenarios. Examples of transients include liquid-metal heat pipe frozen start-up, power transients during normal operation, recovery from heat pipe limit, the cascading failure of multiple heat pipes, and system level transients. Many works have investigated heat pipe response to changes in evaporator input power or condenser cooling rates [62-64], to transients in systems with heat pipes as components [65, 66], and to heat pipe start-up [43, 45, 67-69].

2.4 Life Tests

Life tests may be required to assess long-term reliability concerns related to the compatibility of materials (e.g., heat pipe casing, wick, working fluid), as well as manufacturing methods [70-72]. These tests are imperative when material combinations that have not been tested previously are utilized in the designs. Incompatibilities can cause corrosion and the generation of non-condensable gasses that could diminish performance [73]. Life tests can be of various forms; however, a systematic approach was presented by Martin and Reid who described techniques to shorten the testing time [74]. They proposed magnifying life-limiting effects by testing at higher operating temperatures and linear evaporator heat input rates. In addition, they proposed the extrapolation of corrosion metrics based on life tests of multiple specimens over different testing durations. These corrosion metrics can be identified as heat pipe casing and wick integrity, species distribution, grain boundary conditions, and the amount of non-condensable gasses measured by residual gas analysis [74]

2.5 Instrumentation

High-temperature operation and the presence of liquid metals create a multitude of challenges for instrument integration to test facilities, including difficulties in taking internal measurements, material compatibility issues, and high-costs. Therefore, liquid-metal heat pipe experiments have mostly utilized wall temperature measurements via thermocouples or other types of external sensors [29], as well as systems to monitor and regulate evaporator power input or temperature. In addition, some have utilized a calorimeter at the condenser to calculate the power that is removed. However, these techniques fail to give crucial information on heat pipe two-phase flow dynamics, such as pressures, liquid/vapor flow velocities, stresses, and flow visuals. Experiments that aid in the R&D of advanced reactors should also exploit cutting-edge technologies and techniques that provide such crucial information or eliminate experimental challenges. Hence, advanced measurement and visualization techniques are currently being developed by multiple institutions [75]. These include fiber-optic temperature and strain sensors [16, 43, 47, 76, 77], infrared (IR) thermography, digital image correlation (DIC) [78], high-speed camera flow visualization and pressure measurements of a surrogate fluid [16, 47, 79, 80], x-ray radiography and tomography [64], and laser spectroscopy techniques [81].

3. HEAT PIPE PHENOMENA OF INTEREST

Although they are seemingly simple systems, heat pipe operation involves numerous physical phenomena of great complexity. To make effective use of the available experimental capabilities, it is necessary to rigorously evaluate the phenomena of interest within the heat pipes. For alkali metal heat pipes with microreactor applications, the possible operating states can be identified as follows:

- **Start-up:** The working fluid, which is initially at a fully or partially frozen state, gradually melts and then evaporates to later travel toward the condenser section.
- **Normal operation:** A heat pipe that is under normal operating conditions exhibits nearly isothermal operation across its active length.
- **Operating limits:** The power throughput is bound by heat pipe operating limits that include viscous, sonic, capillary, entrainment, and boiling limits.
- **Degraded performance:** Heat pipe performance may degrade over its operating life due to internal or external corrosion and wick damage, gradually decreasing its heat transfer efficiency.
- **Acute mechanical failure:** Mechanical failure of the heat pipe casing or the wick may cause total failure of the heat pipe.
- **Shut-down:** The shut-down process must consider the future start-up of the heat pipe for optimum start-up performance.

These states and possible parameters and phenomena of interest that can be measured or observed are described in the following subsections.

3.1 Start-Up

Start-up of a heat pipe involves various physical phenomena. Initially, the working fluid can be in a fully or partially frozen state based on the ambient conditions, and full vacuum conditions may exist within the heat pipe if it is not gas-loaded. As the heat is fed into the heat pipe evaporator, the frozen working fluid melts and wets the wick. The melt front then moves from the evaporator toward the condenser to wet the entire wick region. The evaporated vapor simultaneously flows or diffuses toward the condenser depending on the flow conditions. A schematic visualization of this process is provided in Tournier and El-Genk [68], where the continuum, transition, and free-molecular flow regions are displayed. Early on during start-up, the vapor molecule density may be too low to reach continuum flow. Continuum flow conditions can be determined using the Knudsen number, which depends on the characteristic length-scale of the heat pipe diameter and the working fluid’s mean free path. The ramp rate of the evaporator input power during the start-up process must consider the viscous and sonic limits that are significant at lower operating temperatures observed during start-up. Once continuous circulation of the working fluid is established and the heat pipe is under isothermal conditions, the start-up process is complete.

3.1.1 Melt, Temperature, and Continuum Vapor Flow Fronts

Any form of flow visualization is helpful in understanding and communicating two-phase flow physics. In the context of heat pipes, the three so-called “fronts” representing the presence of an interface can be identified as useful for the visualization of heat pipe operation. These are the melt [68, 82, 83], temperature [43, 47, 84], and continuum vapor flow fronts [68, 83]. The melt front designates the solid/liquid interface that represents the boundary of the melted region. Next, the temperature front can be described as the boundary of the region where the heat pipe temperature is approximately isothermal. Finally, the continuum vapor flow front can be used to separate the region where the vapor phase of the working fluid is under continuum flow conditions as opposed to free-molecular flow, vacuum, or non-condensable gas regions. The location of the continuum vapor flow front cannot be identified with current methods; however, it can be treated somewhat analogous to the temperature front, which can be observed with temperature measurements. The temperature front moves from the evaporator to the condenser during start-up, which is a practical and efficient way of characterizing the start-up of a heat pipe. The temperature front can clearly be seen from Figure 2, which shows steady-state vapor core temperature measurements using a fiber-optic distributed temperature sensor.

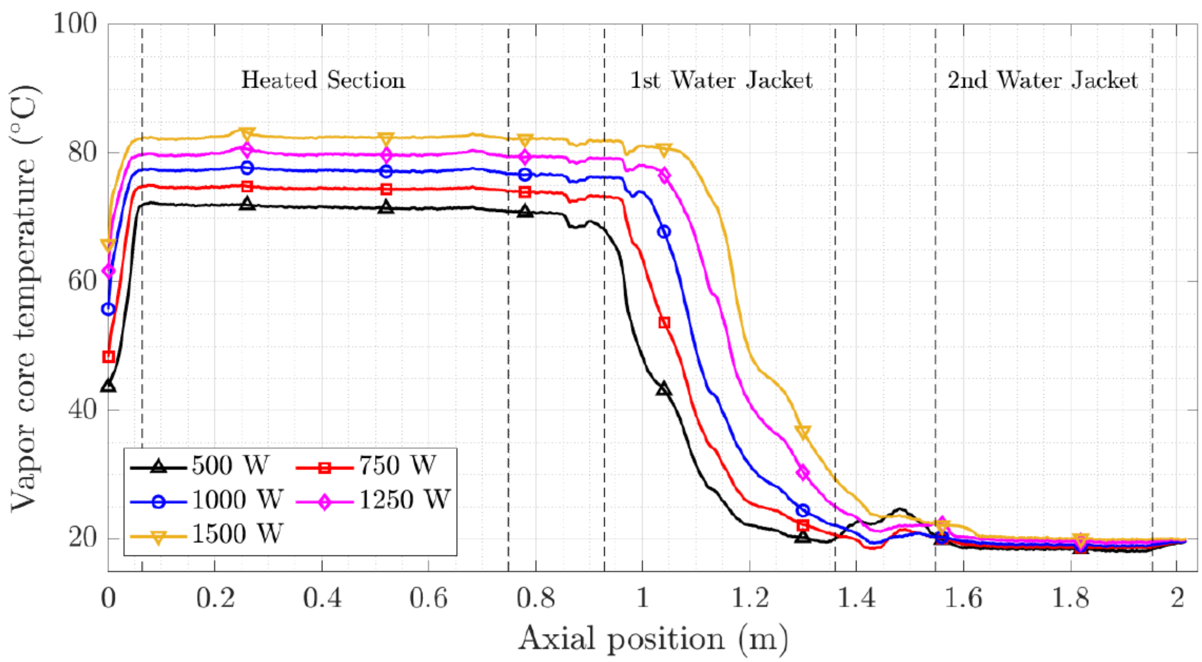

Figure 2. Axial vapor core temperature profiles from Yilgor and Shi [47].

The melt front may be challenging to study with x-ray imaging since one may not be able to distinguish the liquid from the solid due to the relatively low contrast and absorption of sodium compared to the stainless pipe. However, under certain conditions, the movement of the liquid pool toward the condenser section may be observed with x-ray fluoroscopy, given that the test facility is set up for such a technique. Observing the liquid pool as it moves toward the condenser endcap has benefits in characterizing the wick performance during start-up. The pool may also form a plug of excess liquid as it reaches the condenser endcap, which can also be observed with x-ray imaging. The advancement of the liquid pool can be seen in experiments conducted at the University of Wisconsin–Madison (UW–Madison) can be seen in Figure 3.

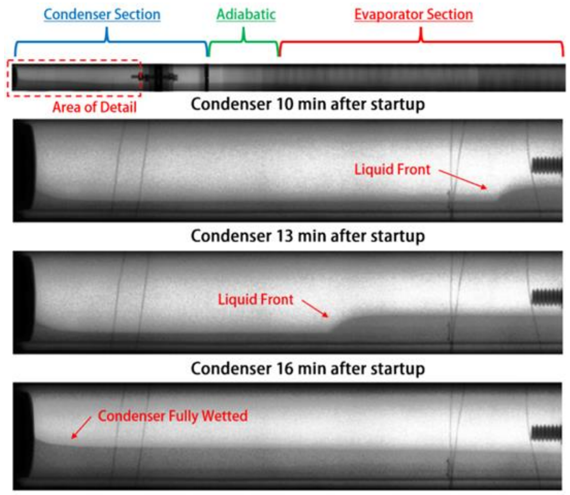

Figure 3. Liquid pool advancement during start-up from Tillman et al. [74].

3.1.2 Time Constant

Rapid response of heat pipes during start-up may be required for certain reactor designs, in which case it becomes important to characterize the time constant of the heat pipe, which is not a strictly defined parameter in literature. However, the heat pipe temperature and location of the temperature front would be practical ways to define a time constant. Additional time constants could also be identified based on the phenomena of interest.

3.1.3 Working Fluid Inventory in the Evaporator

There needs to be some amount of working fluid present in the evaporator section for the proper start-up of a heat pipe. Low working fluid inventory may occur after an improper shut-down of the heat pipe. In the case of low working fluid inventory in the evaporator prior to start-up, large temperature gradients will be seen in the heat pipe wall since the frozen working fluid can only melt after the heat is conducted through the heat pipe wall. This could cause high stresses, which might damage the heat pipe. The working fluid inventory in the evaporator can be observed and its amount measured via x-ray radiography.

3.1.4 Stress/Strain

Greater thermal gradients are more likely to be observed during heat pipe start-up as the heat pipe's heat transfer efficiency may not be as high as in normal operation. Furthermore, the interface between the heat source and the heat pipe may cause additional stresses due to the difference in the thermal expansion of different materials. Both stress and strain can be measured with conventional or distributed sensors.

3.2 Normal Operation

Heat pipes under normal operating conditions operate passively and without any operator action. However, heat pipes need to be monitored continuously to detect any degradation in performance or failures—both for the heat pipes themselves and for the system at large.

3.2.1 Overall Thermal Resistance

One of the simplest ways to quantify heat pipe performance is to investigate the overall thermal resistance of the heat pipe (i.e., the thermal resistance between the heat source, such as the fuel or heater block, and the heat sink, such as the coolant at the condenser). The overall effective conductivity is also used for similar purposes. The thermal resistance can be computed from temperature measurements at multiple locations. It may increase due to a heat pipe limit being reached, which usually transpires as an abrupt increase in evaporator temperature. In addition, the contact resistance at the evaporator or condenser interface might increase due to corrosion or other mechanical degradation, which will in turn increase the overall thermal resistance.

3.2.2 Axial Temperature Profile

The axial temperature profile can be used to clearly visualize heat pipe isothermal operation, while also allowing the identification of the active region of the heat pipe. Furthermore, it is a simple way of observing transients, and of determining whether steady-state is reached. The effectiveness of the heat pipe in a particular application can often be judged using axial temperature profiles. The measurements are usually taken at the wall or the vapor core. The wall measurements often involve thermocouples that are welded or mechanically secured on the heat pipe or in grooves machined along the heat pipe. Vapor core measurements can be taken within integrated thermowells in the heat pipe. Advanced instrumentation such as fiber-optic distributed temperature sensors and ultrasonic temperature sensors can provide very high spatial resolution axial temperature profile measurements.

3.2.3 Location of the Wet Point

The wet point is defined as the axial location where the liquid and vapor pressures are equal. It can also be described as the point where the wick is flooded (i.e., the liquid-vapor interface is flat). Its location depends on numerous factors that include heat pipe orientation and pressure drops. Knowing the exact location of the wet point allows better characterization of the length of the liquid flow path, which is important for the modeling of liquid/vapor flow and pressure drops. The wet point can also be observed with x-ray radiography.

3.2.4 Heating/Cooling Power

Knowledge of the actual power input/output to and from the heat pipe enables the calculation of heat losses, which tend to be significant particularly for high-temperature heat pipe experiments due to both radiative and convective losses. Without rigorous quantification of heat losses, the obtained data may not be effectively used for model verification and validation. The losses can be quantified by comparing heating power to cooling power; for non-nuclear high-temperature test beds, this is usually achieved via watt transducers and gas-gap calorimeters, respectively. The measurements could be supported by analytical estimates of radiative and convective losses from the insulation. Gas-gap calorimeters may also be placed on each heat pipe section, which allows a more rigorous quantification of heat losses [7].

3.3 Degraded Performance

Performance degradation in heat pipes over long-term operation can occur due to numerous effects such as internal/external corrosion, introduction of non-condensable gasses due to oxidation or leakage, wick degradation, and creep at high temperatures. It can usually be identified from temperature measurements. For instance, depending on the conditions, the heat pipe may transfer the expected power at a higher evaporator temperature, which indicates the overall thermal resistance of the heat pipe has increased from designed levels. This could occur due to oxidation at the heater or coolant interface, or by other means as described in the following subsections.

3.3.1 Introduction of Non-Condensable Gasses

Non-condensable gasses may be introduced in the heat pipe due to corrosion or leakage. Their presence can be indirectly observed from axial temperature profiles, given that the measurements have sufficient spatial resolution, since their presence will shorten the isothermal length of the heat pipe as they accumulate at the condenser end. They may also have detrimental effects on the operation of the heat pipe by: (1) increasing the pressure within the heat pipe, as well as the heat pipe operating temperature; (2) causing blockages within the wick if they get trapped, which can obstruct the liquid flow; and (3) altering the thermal coupling at the condenser, which can affect the operating limits. They will, at the very least, cause changes in the normal operating conditions of the heat pipe.

3.3.2 Wick Damage or Degradation

The wick could get altered or damaged during normal operation due to factors such as corrosion, clogging, or mechanical degradation, which can diminish the performance of the heat pipe. Depending on the type and thickness of the wick, corrosion can cause significant damage to the wick structure. Any break in the continuity of the wick structure could limit the capillary pumping ability of the wick. Similarly, any clogs in the wick structure due to corrosion or other contaminants will increase the pressure drop in the wick and could also limit its capillary pumping ability. Other forms of mechanical degradation may occur due to the thermal expansion of the wick, the heat pipe endcaps, and the casing. Wick degradation can be investigated via x-ray radiography during operation, as well as higher resolution computerized tomography (CT) scans post-operation.

3.3.3 Stresses During Long-Term Operation

Thermal and mechanical stresses in the long-term can result in the creep failure of the heat pipe or other system components, which might cause catastrophic failure or otherwise degrade performance. These stresses can be measured with conventional and distributed stress/strain sensors; however, other forms of inspection may be needed for their accurate characterization.

3.4 Shut-Down

Heat pipe shut-down, similar to start-up, involves a multitude of physical phenomena. During shut-down, the working fluid transitions from being in its liquid and vapor states to its solid state under standard atmospheric conditions. The shut-down mechanics depend highly on the power ramp down rate at the evaporator, as well as the cooling conditions at the condenser.

3.4.1 Solidification Front and Solid Accumulation Region

The solidification front can be defined as the solid/liquid interface that represents the boundary of the frozen solid region. How the solidification front behaves depends on the evaporator and condenser conditions during shut-down and the orientation of the heat pipe. Most importantly, if the solid accumulation region is largely outside of the evaporator, there may not be enough working fluid inventory in the evaporator for proper start-up of the heat pipe. Both the solidification front and the solid accumulation region may be observed with x-ray radiography images.

3.4.2 Temperature Front

The behavior of the temperature front during shut-down highly depends on the heating and cooling conditions at the evaporator and condenser. For instance, if the evaporator heat source is shut-down and the condenser is cooled slowly, a heat pipe that is not gas-loaded may largely cool isothermally while the operating temperature is high enough for the working fluid to maintain the cyclic evaporation and condensation. Conversely, for a high enough condenser cooling power relative to the evaporator input power, liquid may pool in the condenser and potentially freeze while the temperature front moves gradually from the condenser endcap to the evaporator, mirroring the temperature front behavior during start-up. Thus, the temperature front during shut-down may be strongly influenced by the melt and continuum vapor flow fronts. In addition, for a gas-loaded heat pipe, the temperature front during shut-down may mirror that of the start-up depending on the cooling conditions.

The temperature front reflects the active heat transfer region during shut-down and can be used to determine when shut-down is complete (i.e., when heat is no longer transferred via the phase-change of the working fluid). The temperature front can be investigated with axial temperature profile measurements.

3.4.3 Shut-Down Time Constant

Similar to the start-up time constant, the shut-down time constant can be used to characterize the timescale for heat pipe shut-down. The parameter may be particularly important if the experiment simulates reactor shut-down or decay heat scenarios. It could be defined in various ways, with a simple way being temperature measurements as in the start-up time constant.

3.4.4 Stress/Strain

Greater thermal gradients can also be significant during shut-down, resulting in higher stresses. These stresses could be due to varying evaporator and condenser conditions, as well as changing geometric dimensions due to thermal expansion. They can be measured with both conventional and distributed stress/strain sensors.

4. REVIEW OF RECENT EXPERIMENTS

A diverse group of U.S. institutions are involved in recent experimental work related to heat pipes. These include Idaho National Laboratory (INL) [1, 19-21, 75, 85], LANL, the National Aeronautics and Space Administration (NASA) [8, 86-93], Rensselaer Polytechnic Institute (RPI) [16, 47, 54, 79, 80, 94], Texas A&M University (TAMU) [33, 43, 52, 53, 75], University of Michigan (UM) [64, 95, 96], and University of Wisconsin-Madison (UW) [97, 98]. These institutions have taken a variety of different approaches in their respective experiments. This paper aims to review the works produced by these institutions.

4.1 Kilopower Reactor Using Stirling Technology (KRUSTY)

4.1.1 Reactor Description

NASA is committed to advancing heat pipe technologies for applications in spacecraft thermal management and fission surface power. Among its flagship projects is the Kilowatt Reactor Using Stirling TechnologY (KRUSTY), which represents a significant milestone in their nuclear program and the development of HPMRs. KRUSTY is designed in partnership with the National Nuclear Security Administration (NNSA), LANL, Y-12 National Security Complex, and Nevada National Security Site (NNSS) to demonstrate a Kilopower space nuclear reactor, which is intended to generate power in the range of 1–10 kilowatt electrical (kWe) [8].

During early stages of the KRUSTY project, three main objectives were established: (1) to operate the reactor concept under steady-state conditions with a 4 kilowatt thermal (kWth) power at a temperature of 800℃, (2) to verify the stability and load during normal and off-normal conditions, and (3) to benchmark the nuclear codes and material cross-sections using experimental data. The project's inception dates to 2015, commencing with a crucial technology demonstration as its' initial step [87, 88]. Following the successful proof-of-concept completed in 2012, NASA's dedicated team spent 3.5 years developing a power system capable of undergoing electrical testing within their facilities. Subsequently, the system was transferred to the DOE facility for nuclear fuel testing.

The Kilopower reactor concept features a cylindrical core utilizing a 32-kg highly-enriched uranium (HEU) alloy enriched with 8% molybdenum, boasting a density of approximately 17.4 g/cm^3 at room temperature. The core's dimensions are 11 cm in diameter and 25 cm in height [89, 91, 93]. Encircling the core is a beryllium oxide (BeO) reflector, which includes an annulus to house a boron carbide (B4O) control rod. Furthermore, eight sodium heat pipes are firmly attached to the fuel via a shrink fit, facilitating efficient heat removal from the core [93]. The design showing the reactor core, power conversion system, and heat pipe radiator is shown in Figure 4. NASA's dedicated efforts in developing this advanced technology hold the promise of revolutionizing power systems for long-term space missions.

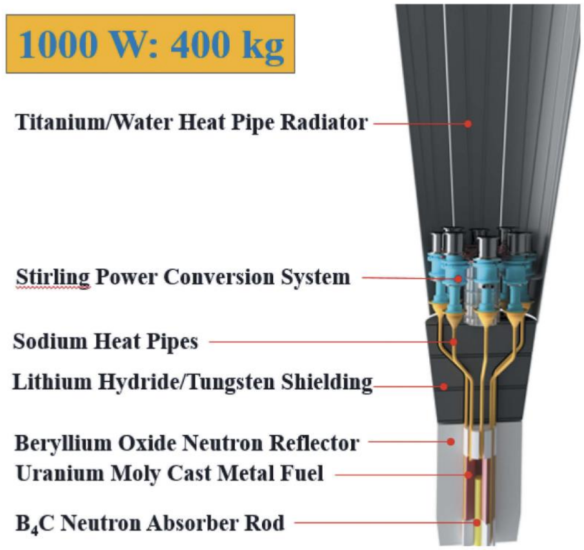

Figure 4. KRUSTY reactor design [8].

The heat pipes are built of Haynes 230 material, which is a nickel-chromium-tungsten-molybdenum alloy designed for high-temperature applications. They included a wick only in the evaporator and the pool/reservoir region for rapid and inexpensive fabrication [92]. The amount of working fluid in the heat pipes is modified based on sodium's neutron reflecting properties. Stirling engines are coupled to each heat pipe for power conversion, and the waste heat is removed via a Titanium heat pipe radiator filled with water as the working fluid. The choice of titanium as the material for the radiators is its lower density compared to similar materials [99].

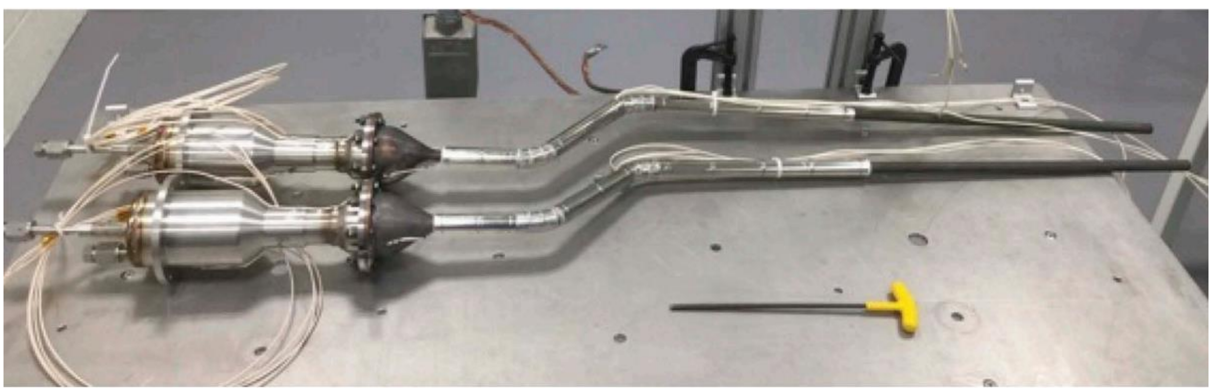

Figure 5. KRUSTY heat pipes coupled to Stirling thermal simulators [100].

4.1.2 Nuclear System Test

The KRUSTY reactor, being the first heat pipe-cooled reactor ever developed, is crucial for the demonstration of heat pipe technology for microreactor applications. The lessons learned from KRUSTY on how heat pipes behave within a reactor system and how they interact with other reactor components is bound to shape the R&D for other HPMRs. The KRUSTY nuclear system test [92] was also first of its kind, as it presented data on heat pipe operation in a real reactor environment that included transients. The comprehensive tests included cold start-up, Stirling power conversion system (PCS) start-up, load-following transients, fault tolerance transients involving failed Stirling modules, and reactivity control transients, as well as loss/restoration of active heat removal. Overall, the reactor operated for 24 hours at temperatures exceeding 800°C, establishing HPMRs as an effective reactor technology.

The start-up of the reactor is briefly summarized here. Initially, the fuel temperature rose without significant heat removal from the heat pipes until the working fluid was fully melted and the operating temperature increased to reach higher viscous limits. Viscous limits typically govern the start-up of high-temperature liquid alkali metal heat pipes from a frozen state [7]. Heat pipes started providing significant cooling power at ~ 500°C, limiting the rate of temperature rise of the fuel. However, they were still bound by the flooding limit due to the absence of a wick structure outside the evaporator. The heat pipe thaw front advanced toward the condenser, with the entire heat pipe reaching a temperature above 500°C within around 20 minutes. At this point, the heat pipe reached isothermal operation and the oscillations in the temperature measurements ceased. The heat pipe temperature then continued to increase, moving away from the viscous limit as it approached nominal operating conditions. It was observed that the individual heat pipes had some differences in temperature as they approached nominal conditions. The tests then proceeded with starting the Stirling converters while the heat pipes operated normally.

The details for the rest of the test can be found in Poston et al. [92]. However, some important findings regarding heat pipes are presented here. The work ultimately found that: (1) heat pipes are effective in reliably removing core power, (2) low-temperature operating limits are an important factor governing HPMR start-up, (3) these heat pipe limits can moderate an uncontrolled power increase in a load-following reactor, and (4) the heat pipes rapidly respond to the reactor transients.

4.2 Single Primary Heat Extraction and Removal Emulator (SPHERE)

4.2.1 Facility Description

INL has supported HPMR development through initiatives such as the design of the Special Purpose Reactor (SPR), the SPHERE experimental facility [21], the Microreactor Agile Non-nuclear Experimental Test (MAGNET) bed [101], and the multiphysics-based heat pipe simulation framework, Sockeye [30, 31, 102]. This section focuses on SPHERE, as it has recently been the main heat pipe facility at INL. It was built to support non-nuclear thermal and integrated systems testing to advance heat pipe technology, improve the understanding of heat pipe operation, and support modeling efforts [21, 30].

The test bed characteristics include 20 kW electrical heating capacity including six silicon controlled rectifier (SCR) power controllers, a gas-gap calorimeter cooled with water for heat rejection, and vacuum or inert gas atmosphere capabilities within the test chamber. A schematic of SPHERE can be seen in Figure 6, where the test article can be seen enclosed in a stainless steel chamber to establish the desired vacuum/inert gas atmosphere and to prevent heat loss to surroundings. Heating can be achieved via a variety of methods. Although the primary heat source has been cartridge heaters, other capabilities include ceramic fiber heaters and induction heaters. Both heater powers and heater temperatures can be controlled. The power inputs to the heaters are monitored using watt transducers. In addition, the heat trace is wrapped around the insulation in the evaporator and adiabatic sections to minimize heat losses. The heat trace is controlled through similar means as described above, but within a separate box equipped with an SCR and proportional-integral-derivative (PID) controller. Since the heat trace is exclusively used for temperature control, the actual heater power is not monitored.

As stated above, the system is also equipped with a gas-gap calorimeter for heat rejection. The calorimeter uses a 5 kW chiller to remove the heat. The chiller pumps water through a differential temperature transducer to record the difference in temperature between the inlet and outlet of the calorimeter, along with a turbine flow meter to calculate the cooling power. A schematic of the calorimeter can be found in Figure 7.

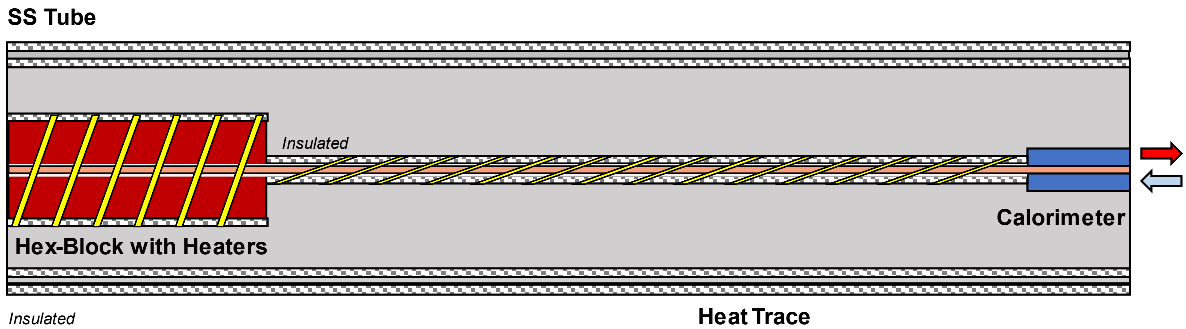

Figure 6. A schematic of the SPHERE facility [76].

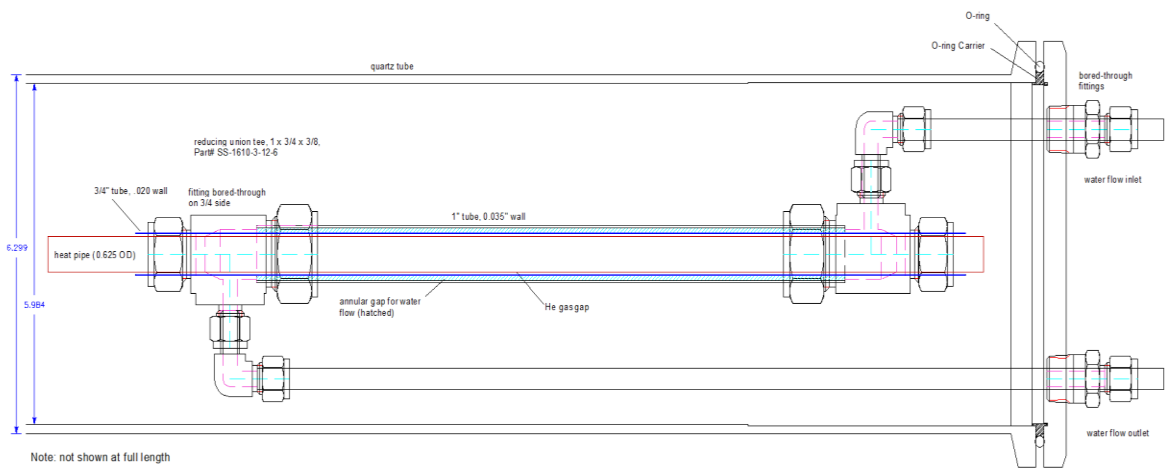

Figure 7. A schematic of the SPHERE gas-gap calorimeter.

The instrumentation capabilities of SPHERE comprise numerous temperature sensors, including traditional thermocouples (TCs), multipoint TCs, fiber Bragg grating (FBG) sensors, optical frequency domain reflectometry (ODFR) distributed temperature sensors (DTSs), ultrasonic thermometers (UTs), and IR thermometry. These advanced instruments are utilized in slots in the heater block or are embedded to the heater block. In addition, fiber-optic strain sensors can also be used along with conventional strain gauges. Overall, a combination of these instruments can be used to measure temperature and strain throughout the heat pipe wall and heater block, as well as in a thermowell if available in the heat pipe.

To date, two major experiments have been conducted using SPHERE: (1) the testing of a heater block with embedded sensors manufactured by ORNL [103], and (2) gap conductance tests to quantify the thermal resistance between the heater block and the heat pipe [76]. These tests are reviewed in detail in the following sections.

4.2.2 Investigation of Advanced Instruments and Embedded Sensors

In collaboration with Oak Ridge National Laboratory (ORNL), INL tested a simulated microreactor core block with several sensors embedded into the block. The tests aimed to demonstrate the reliability of embedded sensors for microreactor applications. Measurements included strains that are caused by thermal gradients and thermal expansion of dissimilar materials present in the block. In addition, the tests quantified the operating limits of heat pipes under a variety of different specifications. ORNL utilized two types of fibers, embedded and floating fibers, along with embedded TCs, which are approximately in line with the fibers. The fibers were a mixture of strain and temperature sensors. Figure 8 showcases the location of the sensors within the block [103].

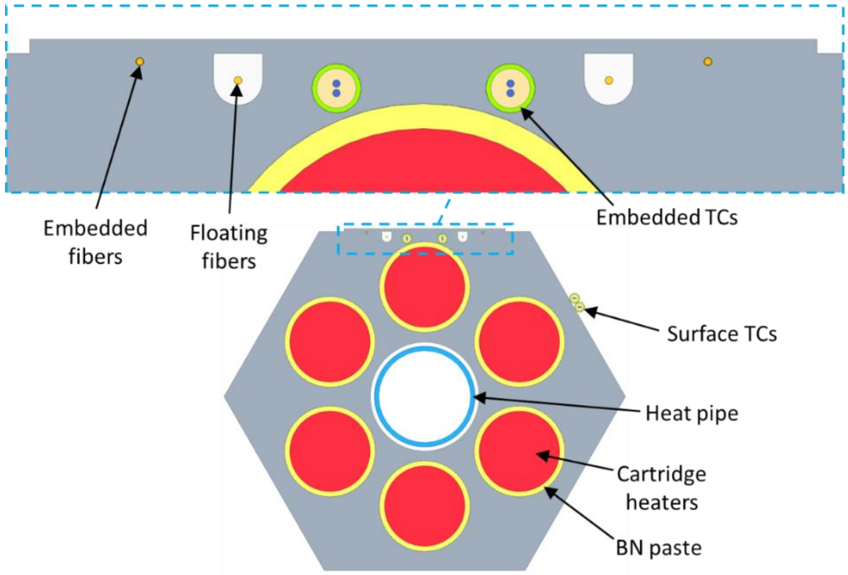

Figure 8. Cross-sectional view of ORNL's embedded sensor block [103].

This setup was installed in INL's SPHERE facility. The system was heated using six 1,000 watt (W) cartridge heaters. These heaters were slotted into the heater holes shown above in Figure 8. Boron nitride paste was used to improve the thermal interface between the heaters and the block. A heat pipe fabricated by Advanced Cooling Technologies (ACT) was slotted down the center hole. Kanthal wire was spot-welded on the outer wall of the heat pipe to act as a centering mechanism. The condenser region of the heat pipe was equipped with a calorimeter for heat removal.

The test was performed by manipulating the temperature of the block by a testing procedure provided by ORNL. This was done by utilizing the PID controllers within the SPHERE control cabinet. These controllers provide input into the SCR power controllers to then provide power to the heaters. The temperature setpoint was updated to match the ramp rates ORNL desired. The test article was ramped to different operating temperatures within the range of operation for sodium-filled heat pipes. This allowed for observation on sensor performance at various operating conditions, and, if a failure occurred, at what point that sensor would fail. Figure 9 demonstrates the testing procedure that was used for this experiment.

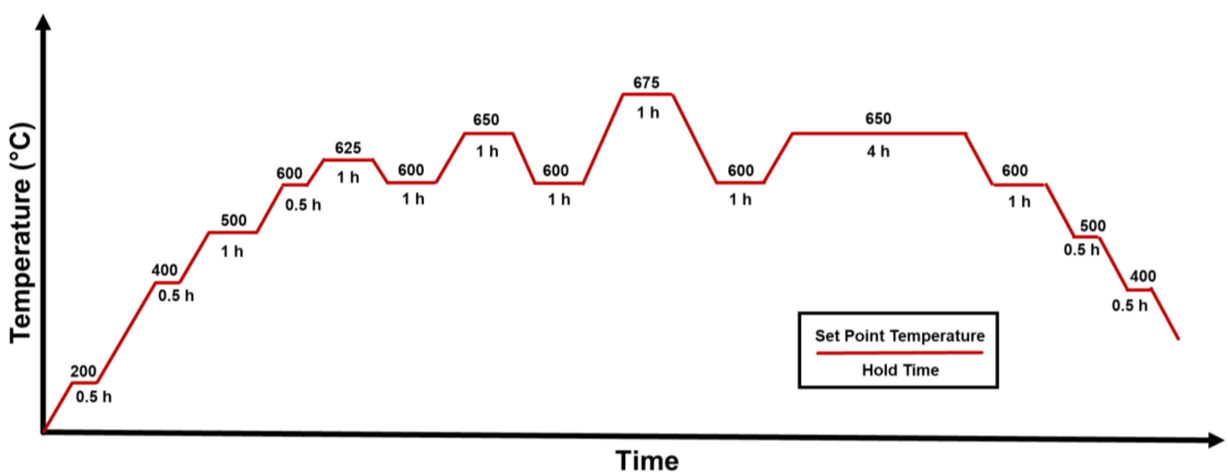

Figure 9. Testing matrix for embedded sensor block [103].

Both the strain and temperature fiber-optic sensors matched the data from the non-embedded sensors. It is worth noting the strain instrument failed at approximately 240°C, but performed well before its failure, matching expected values based on analytical solutions. Figure 10 showcases the strain values obtained during operation, while Figure 11 illustrates the embedded temperature sensors and non-embedded sensors.

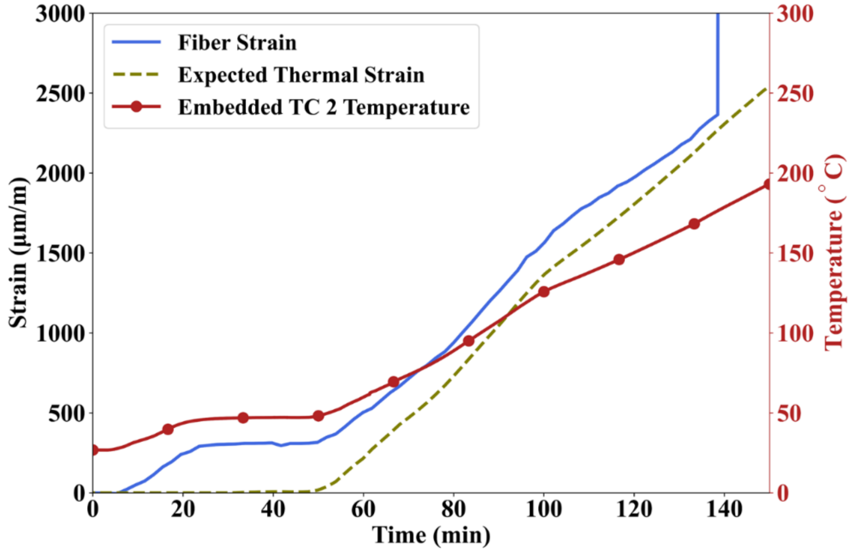

Figure 10. Measured strain, analytical strain, and temperature as a function of time [103].

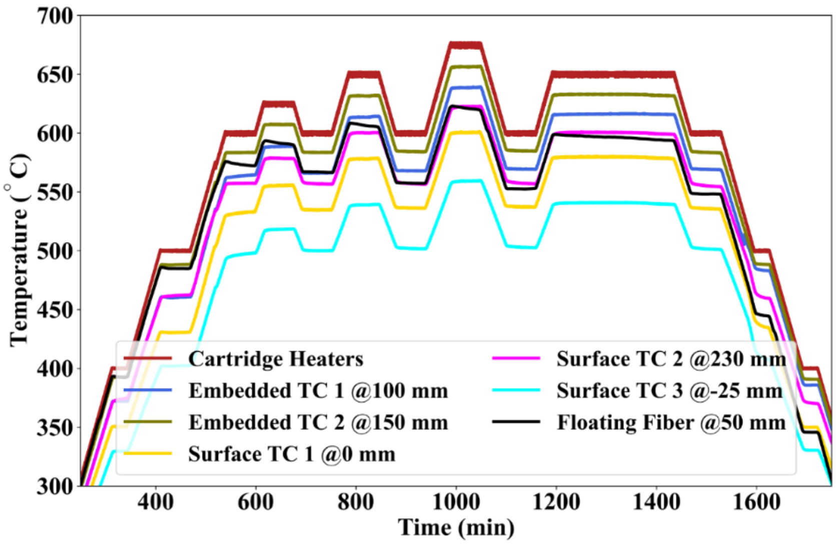

Figure 11. Temperature as a function of time for both the embedded and non-embedded sensor data [103].

The differences in temperature between the sensors depend on a variety of experimental factors. The temperature on the outer sensors are lower than the sensors closest to the heaters because of heat losses from the block. Although the core block was insulated, the system was still losing heat through the outer surfaces due to the high-temperature operation of the system. This effect can be seen in Figure 12, which shows both the system temperature and efficiency of the system, which is characterized by the ratio of the heat removed via the gas-gap calorimeter and the power input to the heaters. This was measured by utilizing SPHERE's calorimeter coupled to the condenser of the heat pipe. The efficiency averages around 20–25%. These results indicate that a majority of the heat was being lost in both the adiabatic region of the heat pipe, as well as the core block [103].

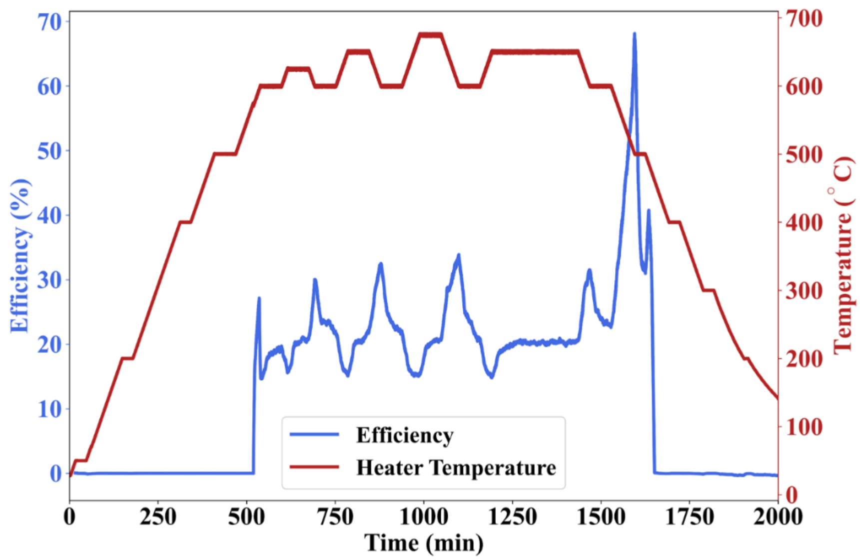

Figure 12. Temperature and efficiency as a function of time [103].

4.2.3 Gap Conductance Tests

Gap conductance tests were conducted to rigorously measure the actual heat flux into the heat pipe at varying gas compositions in the test chamber, which included vacuum, helium, nitrogen, and argon atmospheres. The tests measured the heat rate through the 0.025-in. gap formed at the interface of the heater block and heat pipe. An engineering drawing of the heater block can be seen in Figure 13, showing the location of the multipoint TCs labeled from A-E. The heat pipe test article from ACT included a thermowell into which a multipoint TC was inserted. The locations of the measurement points of the thermowell TC can be seen in Figure 14. The remaining slots along the center bore of the hex block housed two fiber-optic temperature sensors and one ultrasonic temperature sensor. These numerous instruments enable the comparison of measurements at the same axial locations to ensure good contact of the instruments with the heat pipe or heater block.

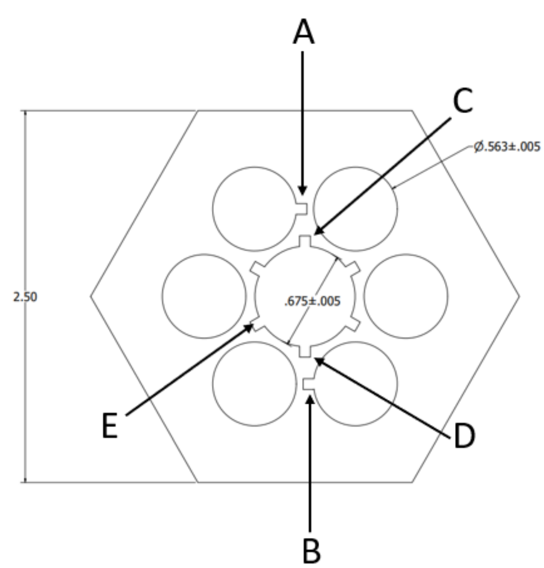

Figure 13. Engineering drawing of the heater block showing the locations of the multipoint TCs in the slots.

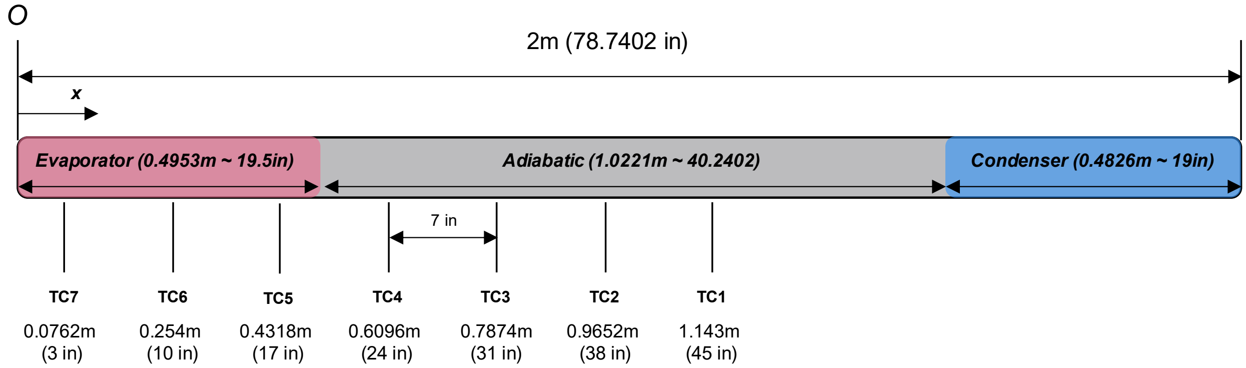

Figure 14. Vapor core temperature measurement locations along the multipoint TC in the thermowell.

Integral junction TCs were also placed on the outside of the core block. These TCs were in line with multipoint TCs A, C, D, and B. The axial positions of these integral junction TCs also matched the embedded TCs, except for the first point. The first point for the multipoint TCs were in line with the front face of the core block with measurement points at every 3-in. intervals for a total of five points. The integral junction TCs allowed for analysis on the heat transfer through the core block via conduction.

The gap conductance testing procedure can be summarized as follows:

1. Purge the test chamber by pulling vacuum and back-filling with the desired gas (e.g., vacuum, helium, nitrogen, argon) for a total of five cycles to minimize the amount of unwanted gasses.
2. Ramp up power to 200 W and hold for 40 minutes.
3. Power up heat trace to achieve a 50°C temperature drop between the outer wall of the heat pipe/heater block and the outer surface of the insulation along the entire heat pipe.
4. Ramp up power to 500 W.
5. When the condenser region reaches 200°C, turn on the chiller in the calorimeter loop.
6. Once at steady-state, increase power to the heat traces to achieve a 50°C temperature drop between the outer wall of the heat pipe/heater block and the outer surface of the insulation along the entire heat pipe.
7. Reduce power to 400 W, and then 300 W, repeating the same procedure as for the 500 W case.

The test shows the heat pipe operating temperature at various powers depends on the gas composition and thermal power. Table 1 showcases the heat transfer rates through the annular gap for the vacuum case for the varying power levels. The vacuum case was also utilized to calculate the emissivity of the system under the assumption the heat transfer is exclusively through radiation. This emissivity value was used to calculate the radiation heat transfer for the different gas compositions (e.g., helium, nitrogen, argon) in the system. Error was introduced to the experiments because the roughing pump that was used to pull vacuum on the system could only pull a rough vacuum of approximately 3400 Pa. The reason for this was that the ceramic fiber insulation stored gasses in its pores that were challenging to remove. The gasses present resulted in 2–3% of the total heat transfer rate to be via conduction. These values closely matched the expected results for the input through the core block into the heat pipe. It was previously estimated that up to 50% of the total power input would be lost to the environment through the core block. It was also shown that nearly all the heat transfer for the vacuum case was radiative heat transfer, which is consistent for vacuum operation.

Table 1. Heat transfer rate for vacuum case.

	Power [W]		
	500	**400**	**300**
T_{GAP} (= T_D) [K]	1046.15	983.15	923.15
T_{HP} [K]	994.15	935.15	882.15
q_{rad} [W] (ε = 0.73, Eq. 1)	176.84	135.67	96.58
q_{cond} [W] (k_{air} = 0.0025 W/m-K, Eq. 2)	3.88	3.58	3.06
Total q_{gap} [W]	180.72	139.25	99.64
q_{cond}/q_{gap} [%]	2.15	2.57	3.07

As expected, the cases with gas atmospheres had higher conduction heat transfer rates. The total heat transfer rate was a function of the thermal conductivity of the gasses as well as the varying power levels of the system. Table 2 through Table 4 illustrate the heat transfer rates for the different gas atmospheres. The radiative heat transfer for the helium case was significantly lower than the other cases due to the higher thermal conductivity of the gas. The overall temperature of the system was approximately 150–200 degrees lower than for other gas compositions. Furthermore, as can be seen in Table 1 through Table 4, the ratio of the conduction heat transfer to total heat transfer increases with decreasing input power. This increase can be attributed to lower operating temperatures resulting in a higher radiation thermal resistance.

Table 2. Heat transfer rate for helium cases.

	Power [W]		
	500	**400**	**300**
T_{GAP} (= T_D) [K]	837.15	816.35	794.15
T_{HP} [K]	818.15	803.15	784.94
q_{rad} [W] (ε = 0.73, Eq. 1)	34.49	22.44	14.51
q_{cond} [W] (k_{He} = 0.3 W/m-K, Eq. 2)	170.29	118.31	82.55
Total q_{gap} [W]	204.78	140.75	97.06
q_{cond}/q_{gap} [%]	83.16	84.06	85.05

Table 3. Heat transfer rate for nitrogen cases.

	Power [W]		
	500	**400**	**300**
T_{GAP} (= T_D) [K]	960.61	901.10	848.90
T_{HP} [K]	910.12	856.09	814.27
q_{rad} [W] (ε = 0.73, Eq. 1)	132.37	97.79	63.77
q_{cond} [W] (k_{N2} = 0.05 W/m-K, Eq. 2)	75.43	67.24	51.73
Total q_{gap} [W]	207.80	165.02	115.50
q_{cond}/q_{gap} [%]	36.30	40.75	44.79

Table 4. Heat transfer rate for argon cases.

	Power [W]		
	500	**400**	**300**
T_{GAP} (= T_D) [K]	1012.37	949.22	888.03
T_{HP} [K]	961.75	901.08	840.38
q_{rad} [W] (ε = 0.73, Eq. 1)	155.92	122.11	98.51
q_{cond} [W] (k_{Ar} = 0.03 W/m-K, Eq. 2)	45.37	43.15	42.70
Total q_{gap} [W]	201.29	165.26	141.21
q_{cond}/q_{gap} [%]	22.54	26.11	30.24

These tests were performed to investigate how gap conductance between the heater block and the heat pipe affects operating characteristics. Quantifying the gap conductance is crucial for modeling the thermal coupling of heat pipes to the rest of the core. Thus, the obtained data can be utilized in the validation of models for heat pipe systems—including heat pipes and a core block. The results of this work are in close alignment with predicted behavior for one-dimensional heat transfer for solid bodies. The phase-change heat transfer within the heat pipe itself does not significantly alter the behavior at the block or heat pipe wall.

Future work would focus on improving the guard heating units. This would include upgrading the heat trace wrapped around the adiabatic and evaporator sections of the system. These improvements would provide a higher fidelity comparison between the individual heat pipe element that SPHERE represents, and the larger, full-scale prototypic system of the microreactor concept. In the prototype, there would be hundreds to thousands of such heat pipe elements in the core block. Because of this, the outside surface of the SPHERE's evaporator should be close to adiabatic to better model the actual reactor core design.

4.3 Low-Temperature Heat Pipe Test Facility (LTHPF)

4.3.1 Facility Description

Unlike SPHERE, which was designed for the direct testing of prototype scale heat pipes, the Low-Temperature Heat Pipe Test Facility (LTHPF) was developed at RPI according to previously developed scaling laws [79] to bypass the difficulties of experimenting with liquid-metal working fluids by using surrogate fluids [16]. These difficulties normally include strict safety precautions, skilled labor requirements, as well as high start-up and revolving costs. Furthermore, a more comprehensive experimental database that includes internal measurements and flow visuals can be developed for low-temperature heat pipes. The scaling laws that were used were derived directly from governing equations and constitutive relations of the modeling framework developed by Shi et al. [79, 80].

The test section is scaled-down from the INL SPR [2] to around half its length (e.g., ~ 2 meters) while keeping the diameter approximately identical. Table 5 shows the design parameters of the facility compared to the prototype. The lengths of each heat pipe section are also kept approximately half of the prototype. It should be noted that the LTHPF can house different annulus-screen and wrapped screen wicks that are fabricated in-house at RPI.

Table 5. Design parameters of the prototype and test facility.

Design Parameters	Prototype	LTHPF
Pipe material	SS316	SS316
Wick type	Annulus-screen	Modifiable
Nominal power	4.5 kW	3.5 kW
Pipe inner diameter	15.75 mm	15.80 mm
Pipe outer diameter	17.75 mm	21.34 mm
Pipe flow area	194.8 mm^2	196.1 mm^2
Evaporator length	1.5 m	0.75 m
Adiabatic section length	0.3 m	0.18 m
Condenser length	2.1	1.10 m
Total length	3.9 m	2.03 m

A schematic design of the test facility can be seen in Figure 15. The different sections of the heat pipe are connected using flanges, which allows for modularity and rapid modification of the lengths of different sections. Measurements of temperature, pressure, and film thickness (for thermosyphons) are taken at the two instrumentation ports, along with temperature and pressure measurements at the endcaps. A fiber-optic temperature sensor runs along the entire length of the heat pipe for the high-resolution measurement of axial vapor core temperature profile. In addition, flow visuals can be taken from the two visualization ports in the adiabatic section and condenser. Readers are referred to Yilgor et al. [16] for additional details regarding the design of the test facility.

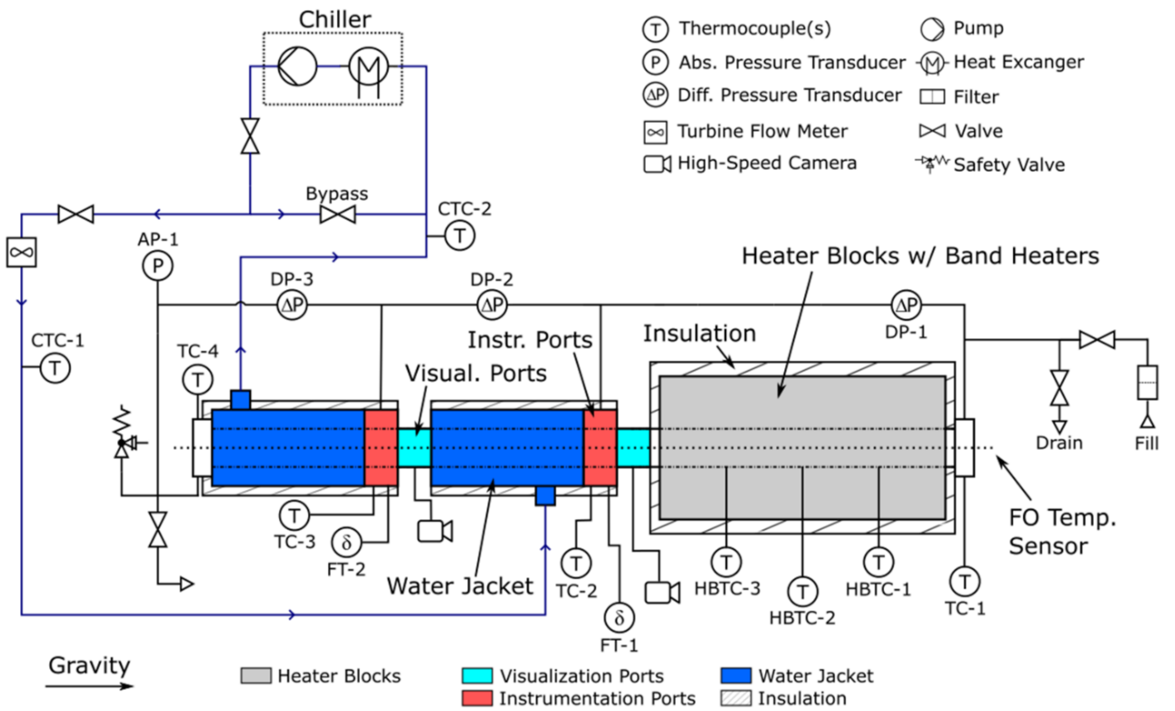

Figure 15. A schematic design of the LTHPF at RPI.

Since surrogate fluids are used, the range of similarity parameters that can be obtained under normal conditions are of paramount importance. The scaling laws developed by Yilgor and Shi yield numerous similarity parameters that can be used to characterize two-phase flow within heat pipes and two-phase closed thermosyphons [79]. These similarity parameters are given in Table 6 and Table 7 for completion, along with the reported ranges for the parameters that can be achieved experimentally in LTHPF. Through these similarity parameters and the quantification of scaling distortions, LTHPF can be used to study specific phenomena of interest in high-temperature heat pipes.

Table 6. Similarity groups that do not change with input parameters because they are geometric or equal to unity at steady-state [16].

Similarity Groups	**Value**
Length to diameter ratio	47.5
Liquid phase-change number	1
Vapor phase-change number	1
Liquid length to hydraulic diameter ratio	221
Vapor length to hydraulic diameter ratio	60.5
Liquid Strouhal number	1
Darcy number	9.45E-05
Liquid phase fraction	0.384
Vapor phase fraction	0.616

4.3.2 Methods and Instrumentation

Yilgor and Shi recently published their first dataset from LTHPF involving 15 different combinations of evaporator input powers and condenser coolant mass flow rates ranging from 500–1,500 W and 0.10–0.20 kg/s, respectively [47]. The power input levels were determined based on an experimentally observed operating limit, which was around 2 kW. The heat pipe included an annulus-screen wick fabricated in-house via spot-welding from SS304 number 400 screen mesh, with the annular gap being imposed by a 0.635 mm (0.025-in) SS304 wire wrapped helically around the screen.

The experimental procedure was designed to obtain steady-state data at the determined evaporator input powers and condenser mass flow rates. The major steps in the procedure can be summarized as follows:

1. Purge pressure lines to remove air bubbles that could cause uncertainties.
2. Adjust working fluid level to the desired fill ratio based on evaporator length.
3. De-gas the test section by boiling at 1 kW input power to remove non-condensable gasses from the heat pipe.
4. Start the chiller system circulation and allow the heat pipe to reach steady-state.
5. Modify the evaporator power input to the desired level for each case.

The dataset consists of heat pipe temperatures and pressures at different operating conditions. The temperature data includes fiber-optic distributed temperature sensor (FO-DTS) measurements of the vapor core along with liquid film and evaporator wall temperature measurements using type-K TCs. The pressure data includes operating pressures, as well as axial pressure profiles. Furthermore, the change in operating pressures and temperatures for the different cases are reported. The work also reports the actual heating power of the heaters, as well as the condenser cooling power.

Table 7. Similarity parameter ranges for the LTHPF using water as a working fluid and an annulus-screen wick [16].

Similarity Groups	Values
Vapor Strouhal number	~ 100–2,000
Liquid Euler number	~ 200–2,000
Vapor Euler number	~ 3
Liquid Reynolds number	~ 100–1,000
Vapor Reynolds number	~ 7,000–22,000
Velocity ratio	~ 5E-4–8E-3
Liquid Froude number	~ 1E-5–3E-4
Vapor Froude number	~ 4–50
Liquid Peclet number	~ 1E+6–2E+7
Vapor Peclet number	~ 4E+7–1E+9
Liquid Prandtl number	~ 1–2
Vapor Prandtl number	~ 1
Liquid Weber number	~ 4E-3–1E-1
Gas Weber number	~ 100–200
Liquid Viscosity number	~ 5E-4–8E-4

4.3.3 Recent Results

The first set of experimental data from LTHPF was published very recently, where the authors focused on steady-state analysis [47]. They investigated 15 different experimental cases with condenser coolant flow rates of 0.10, 0.15, and 0.20 kg/s, and evaporator power inputs of 500, 750, 1,000, 1,250, 1,500 W, respectively. The results for a 0.15 kg/s condenser coolant flow rate case are shown in Figure 16 as an example where the axial pressure, liquid film temperature, and vapor core temperature measurements are given. The vapor core temperature measurements using fiber-optic sensors are demonstrated to yield high spatial resolution data. It should be noted that the work represents the first demonstration of axial pressure profile measurements and fiber-optic vapor core temperature measurements for heat pipes in literature to the best of the authors' knowledge.

It can be seen from the axial pressure profiles shown in Figure 16(a) that the measured pressure decreases in the vapor flow direction and remains relatively constant at the inactive region of the heat pipe. In addition, the pressure profiles are shifted with changing evaporator input power while maintaining their trend. Next, it can be seen from the liquid film temperature profiles shown in Figure 16(b) that the evaporator end cap liquid film temperature exceeds that of the adiabatic section at high-input powers due to the depletion of the liquid pool. Last, the vapor core temperature profiles show exceptionally high-resolution, where the active and inactive regions of the heat pipe can clearly be observed. They also show how the active length expands with increasing input power. It should be noted that no significant difference in the active lengths were observed between the different flow rates for the same power input.

In addition, the operating pressure defined at the condenser end cap and the operating temperature defined at the adiabatic section, are shown in Figure 17. The operating pressure behaves nearly linearly with increasing power for all three condenser coolant flow rates, whereas the operating temperature shows a trend of decreasing marginal increase, which indicates a higher heat transfer efficiency.

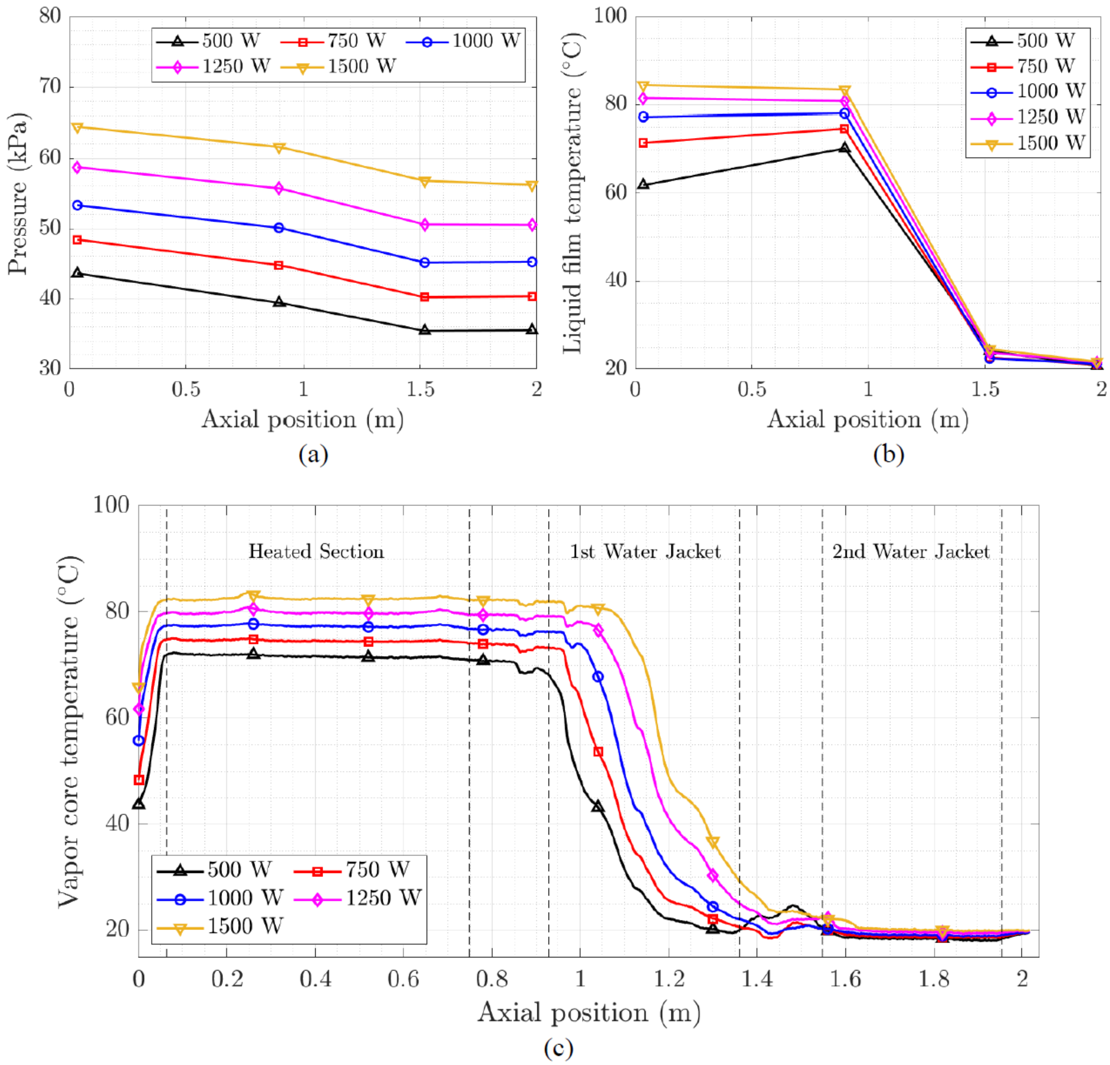

Figure 16. Axial profiles of (a) pressure, (b) liquid film temperature, and (c) vapor core temperature for the 0.15 kg/s condenser flow rate case at steady-state [47].

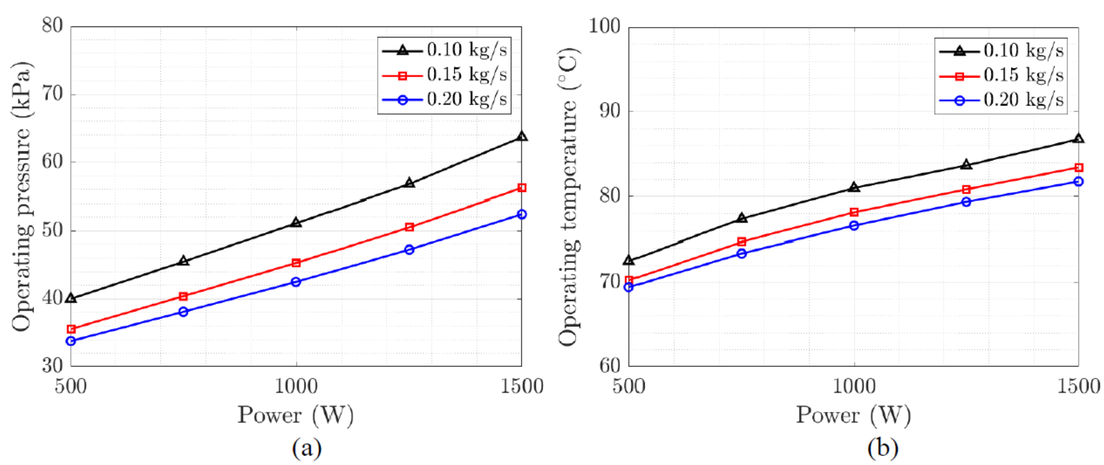

Figure 17. Steady-state values of (a) operating pressure and (b) operating temperature as defined at the condenser endcap and adiabatic section, respectively [47].

4.4 Texas A&M University

4.4.1 Facility Description

Research conducted at TAMU has mainly focused on the characterization and optimization of heat pipes with annular wick structures [43, 52, 53]. The work aims to support the verification and validation (V&V) of numerical tools for HPMRs through internal heat pipe measurements. The experimental facilities include heat pipe test beds, as well as wick characterization rigs, which enable novel wick development, heat pipe performance testing, and flow visualization. The heat pipe manufacturing processes of cleaning, vacuuming, filling, sealing, and wick fabrication are all performed on-site. Some images and a schematic of the horizontal heat pipe test bed can be seen in Figure 18, where the test section without insulation is shown at the top, and the major components of the test facility are shown on the right.

The facility schematic shows the exterior TCs placed throughout the heat pipe, along with a flow meter used for water jacket calorimetry, a pressure gauge at the condenser end that is used to determine vacuum levels within the heat pipe, and a vacuum pump. Four analog pressure gauges are placed in total to measure the inner pressure at the evaporator end cap, evaporator exit, adiabatic exit, and condenser end cap. Evaporator heating is achieved via a fiberglass tape heater wrapped around a copper block, and the condenser is cooled by a water jacket connected to a recirculating chiller. The heater power is controlled by a transformer and a watt transducer.

In addition, a heat pipe visualization test bed was designed to primarily investigate flow structures as opposed to conducting a thermal analysis of the heat pipe. To achieve this, the entire heat pipe is modified to be transparent and to include semi-circular wicks that expose the inner surface of the annular wick for imaging. A glass plate separates a transparent circular tube to form a semi-circular heat pipe, as shown in Figure 19. The heat pipe is placed within a setup that enables the placement of high-speed and IR cameras, and the modification of orientation with respect to gravity from 0° to 90°. These angles represent horizontal and gravity-aided operation, respectively. Images of the setup can be seen in Figure 20 and Figure 21. It should be noted that evaporator heating is achieved via a transparent glass heater to avoid blocking the imaging windows.

Facilities at TAMU also include wick characterization rigs that are used to measure porosity, permeability, effective pore radius, and contact angle [52, 53]. Porosity is measured using an Archimedes or volume-based method where a wick sample is saturated with a fluid with known density, and the porosity can then be computed from the weight difference between a dry and fully saturated sample. The permeability and effective pore radius are measured using a capillary rate-of-rise method [56, 104] where the height of the rising liquid is measured indirectly through the total weight of the rising liquid [53]. The contact angle is measured via a custom optical tensiometer utilizing the sessile drop method.

The instrumentation capabilities at TAMU include conventional sensors such as pressure gauges, TCs, and flowmeters, as well as advanced technologies, such as fiber-optic temperature sensors, high-speed cameras, IR cameras, and confocal chromatic sensors. The fiber-optic measurements utilize a LUNA ODiSI system that can support up to eight sensors simultaneously. The individual sensors can be manufactured in-house through polyamide coated fibers inserted into polytetrafluoroethylene (PTFE) and stainless steel tubes [43].

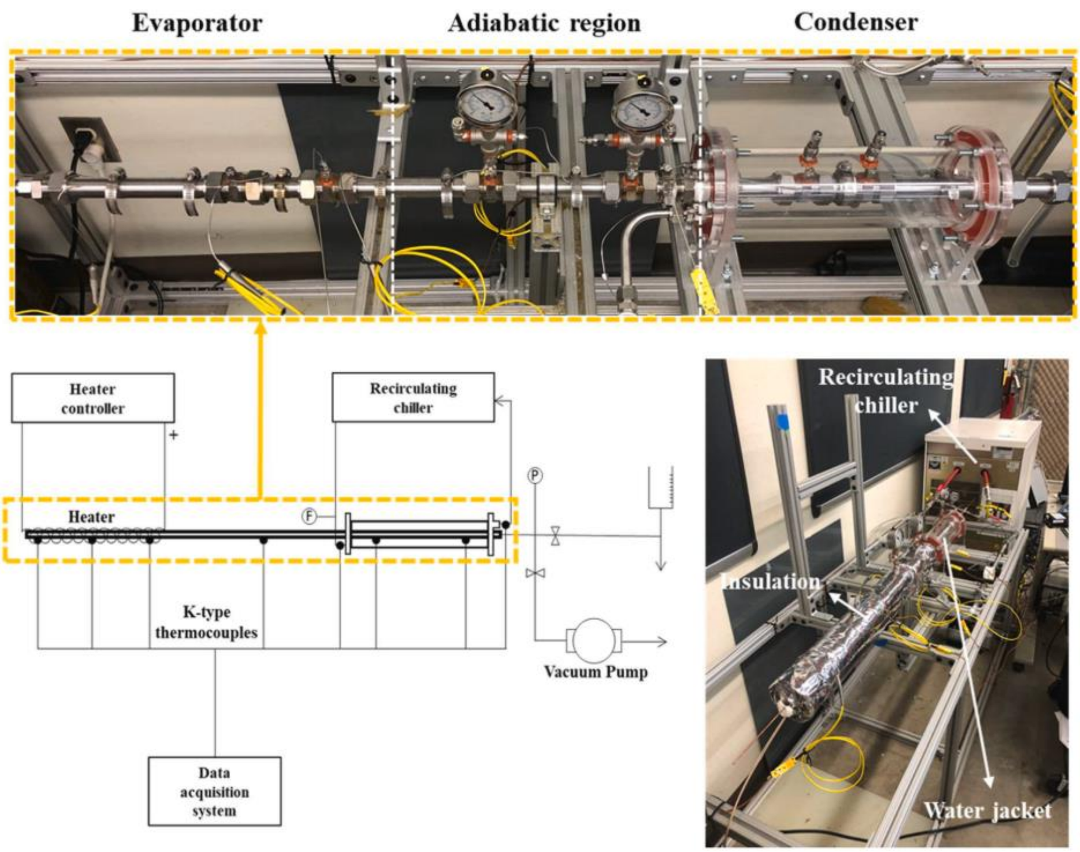

Figure 18. Images and a schematic of the horizontal heat pipe test bed at TAMU.

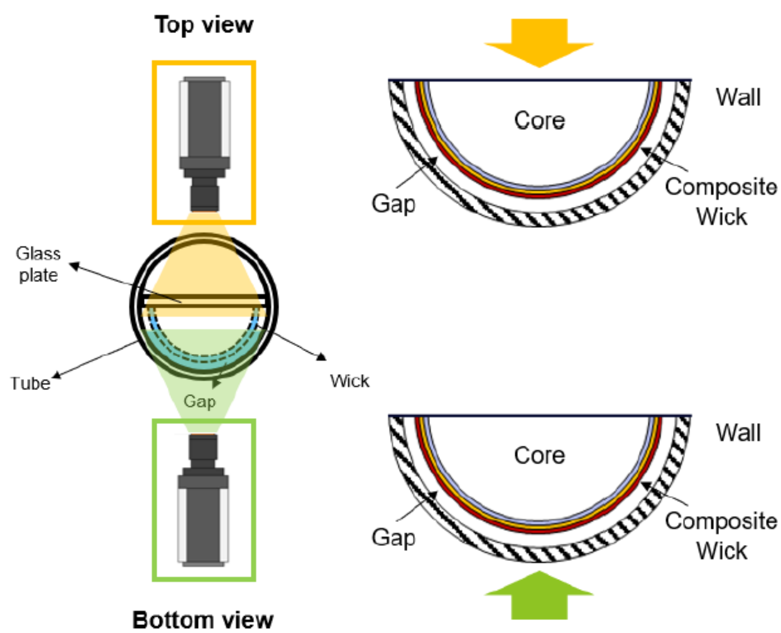

Figure 19. Semi-circular heat pipe and wick developed for the visualization of the inner surface of the wick and the vapor core.

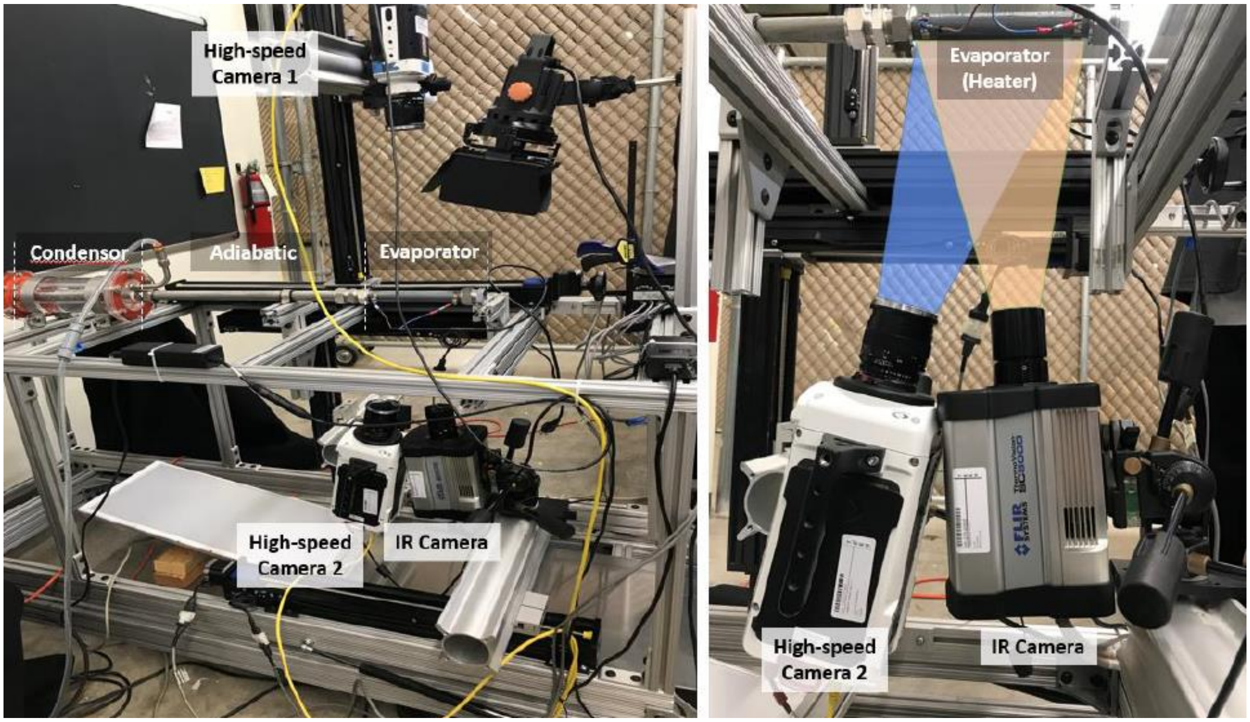

Figure 20. Images of the heat pipe visualization test bed showing the heat pipe sections and the layout of the cameras.

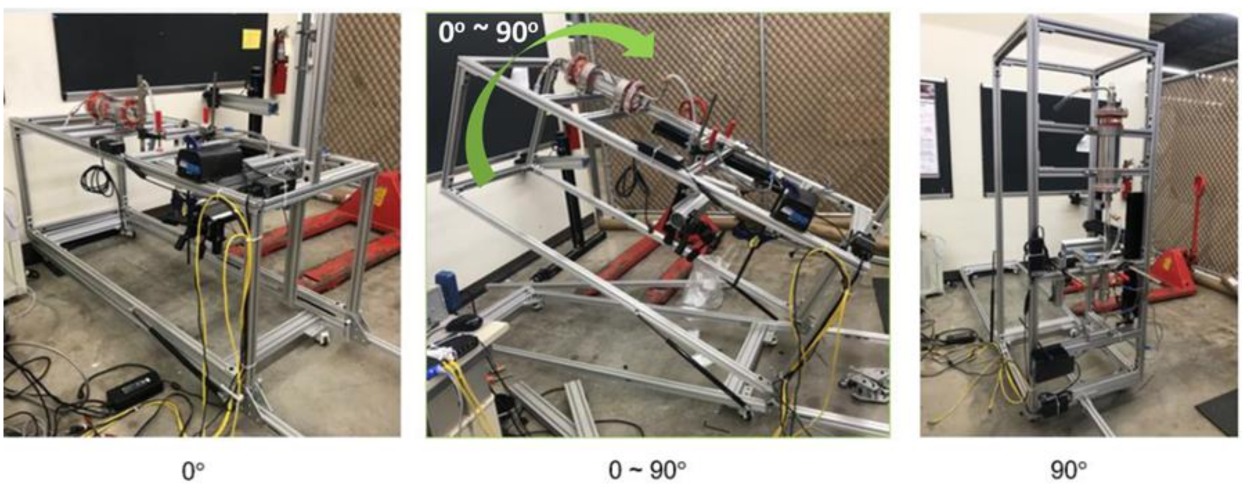

Figure 21. Images of the heat pipe visualization test bed demonstrating horizontal, inclined, and vertical operation.

4.4.2 Wick Development and Characterization

Seo et al. recently investigated composite annulus-screen wicks composed of different pore sizes [53] and the optimization of the annular gap distance [52]. Nine composite wick structures built using number 100, 400, and 60 stainless steel screen meshes at the inner, middle, and outer positions were investigated. Each wick had six layers of screens in total but differed in the screen numbers that were utilized. Twelve samples for each different wick design were built to minimize uncertainties related to the manufacturing process. The porosity, permeability, and effective pore radius of the wicks were measured using wick characterization test rigs mentioned in the previous subsection.

As a result of these wick characterization tests, the wick structure shown in Table 8 was found to yield the highest permeability and permeability-to-effective pore radius ratio (K/r_{eff}). This wick was chosen for heat pipe performance testing as it was expected to provide the highest capillary limit based on the K/r_{eff} ratio that can be used to characterize wick performance [105]. Furthermore, it is known that wicks with relatively high permeabilities are needed for long heat pipes with high aspect ratios to reduce viscous losses [54]. It should be noted that the values listed in the table are for the screens only and does not consider the presence of the annular gap.

Table 8. Parameters of the wick chosen for heat pipe performance evaluation.

Wick Composition			Wick Parameters			
Inner	Middle	Outer	Porosity (-)	Permeability (μm)	Eff. Pore Radius (mm)	K/r_{eff} (μm)
1 × #100 screen	3 × #400 screen	2 × #60 screen	0.653	1.435E-3	0.213	6.737E-3

The chosen wick was then evaluated at different annular gap distances that were imposed using shims. The results can be seen in Figure 22, where the effect of the gap distance on both the permeability and effective pore radius are shown. In this data, "bare mesh" refers to the testing of only the composite screen, whereas the "mesh with gap" includes a wall and a shim to set the gap distance. The conclusions drawn are listed as: (1) even for a gap distance of zero while using a wall, the measured permeability is larger, whereas the effective pore radius smaller, than using just the screens; and (2) an optimum gap distance exists at a distance of around 1.2 mm for water and ethanol, which corresponds to around 11% of the heat pipe's radius.

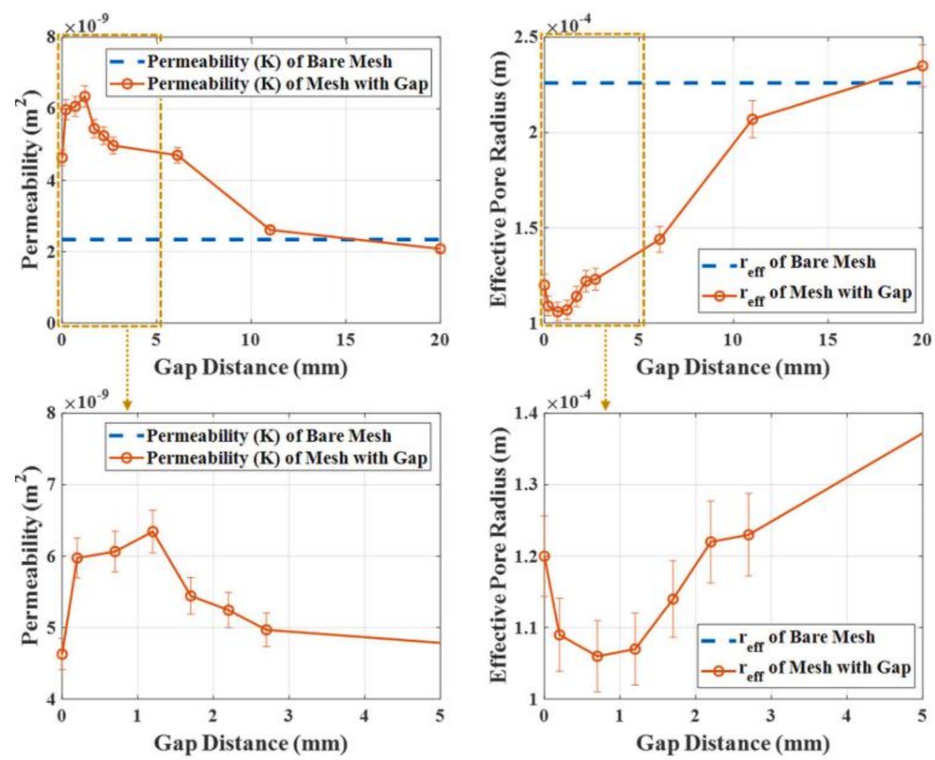

Figure 22. Permeability and effective pore radius with varying gap distance [53].

The reason for the increased permeability and decreased effective pore radius when a wall is introduced is explained through the gap between the screen and the wall providing an additional flow path and capillary pumping ability, even at a gap distance of zero. Thus, it can also be concluded that a wall should be integrated while measuring the permeability and effective pore radius of annular wick structures in order to obtain more accurate characterization results.

Heat pipe performance testing was conducted by applying the desired power input and changing the condenser flow rate to achieve the desired operating temperature. The limit conditions were determined by increasing the evaporator input power while keeping the operating temperature constant until an abrupt temperature rise was observed at the evaporator, which indicated the occurrence of a limit. The heat pipe that was used had the wick described above with a gap distance of 0.95 mm. The results are shown in Figure 23 in the form of a heat pipe operating envelope. It can be seen that the theoretical capillary limit adequately describes the operating limit of the heat pipe. It should be noted that the capillary limit relation used included the liquid viscous pressure drop only.

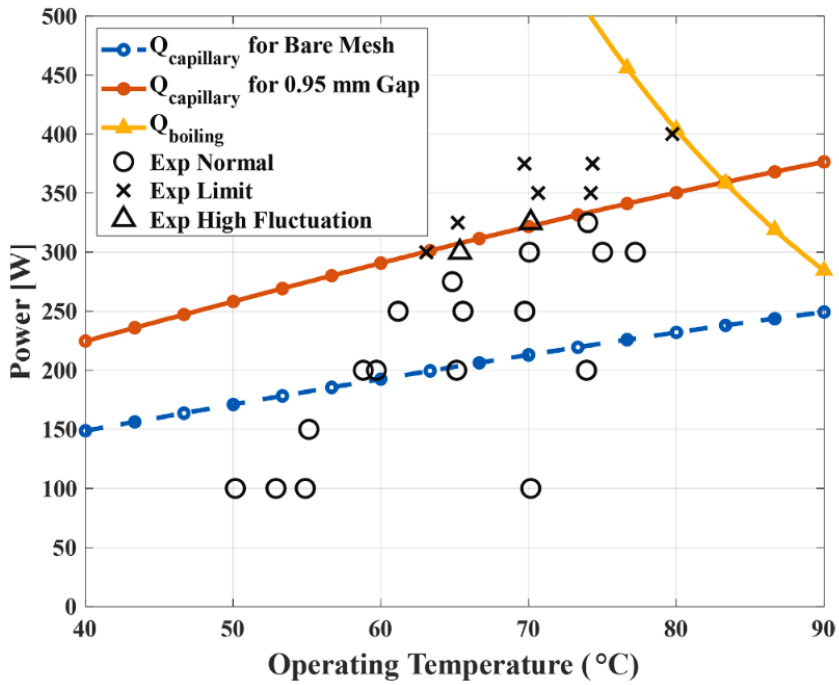

Figure 23. Results from the experiments along with theoretical heat pipe operating limits [53].

In addition to composite wick development, Seo et al. sought to develop an analytical model for the characterization of the capillary performance of annulus-screen wicks with different gap distances [52]. They proposed the use of non-dimensional models describing the capillary rise between two flat plates of dissimilar materials [106, 107] for annulus-screen wick applications. They verified the applicability of this approximation with experiments and found that the relation given by O'Brien et al. [108], which considers the different contact angles of the two dissimilar materials, is appropriate for modeling the capillary rise in an annulus-screen wick structure. They then computed the K/r_{eff} ratio analytically to compare with the data obtained in their aforementioned work [53]. Their results are shown in Figure 24, where it can be seen that the proposed analytical method accurately describes the gap effect. The optimal gap size is defined as the distance at which the highest K/r_{eff} ratio can be achieved. It should be noted that the proposed model can be used for different working fluids and geometries to predict the optimum annular gap distance since a non-dimensional model is utilized. Finally, for HPMR applications, they suggested an optimal gap size of 0.84 mm based on their measurements for a sodium heat pipe with a #100 mesh.

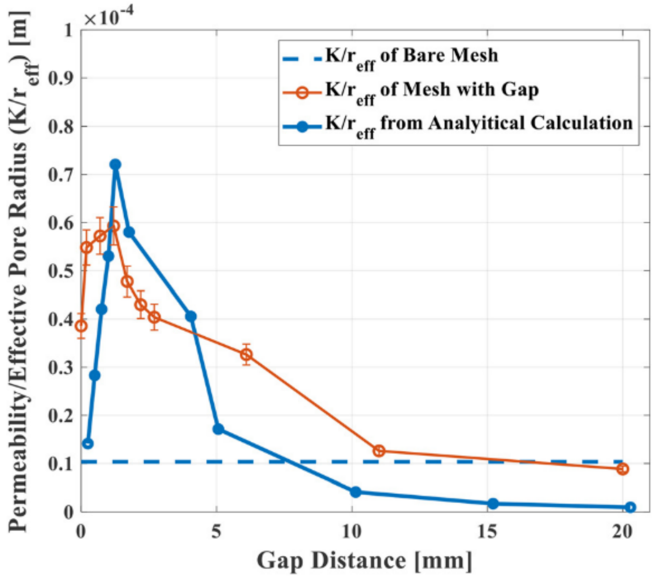

Figure 24. A comparison of analytical capillary performance prediction with experimental data [52].

4.4.3 Investigation of Heat Pipe Start-Up with Fiber-Optic Sensors

As described earlier in the present work, the heat pipe start-up process includes complex phenomena that must be investigated in detail for the V&V of models for microreactor applications. Fiber-optic distributed temperature sensing offers high spatial resolution temperature measurements, which can be utilized to better understand heat pipe start-up. For instance, it can be used to accurately track the location of the temperature front moving from the evaporator to the condenser during start-up. Furthermore, radial temperature differences between the heat pipe outer wall, inner wall, and vapor core region throughout the heat pipe can be measured with the use of multiple sensors.

Seo et al. employed FO-DTS sensors to perform measurements on a 1.2 m long, 22.1 mm inner diameter, horizontal heat pipe utilizing the wick described in Table 8 with an annular gap of 0.95 mm [43]. Start-up at two different heating powers of 30 W and 75 W were investigated, along with the effects of the condenser coolant temperature at 25 W input power. The experiments utilized four FO-DTS sensors to measure axial temperatures at different locations, as shown in Figure 25. Configuration 1 was used for the start-up tests, whereas Configuration 2 was used to investigate the onset of operating limitation. The start-up process took ~1 hour, after which steady-state conditions were observed. It was found that the FO-DTS sensor measurements displayed nearly identical temperatures to the TCs. The sensors allowed the visualization of the temperature front over time as it moved from the evaporator to the condenser end cap.

Data over time in the form shown in Figure 26 is presented for the cases investigated. The major conclusions of the work include: (1) observance of dry out conditions at the evaporator endcap at the high start-up input power, (2) cooling conditions have a strong influence on the temperature profiles, affecting the response speed and the effective length, and (3) large temperature differences up to ~ 45°C were observed between the top and bottom of the investigated horizontal heat pipe under limit conditions.

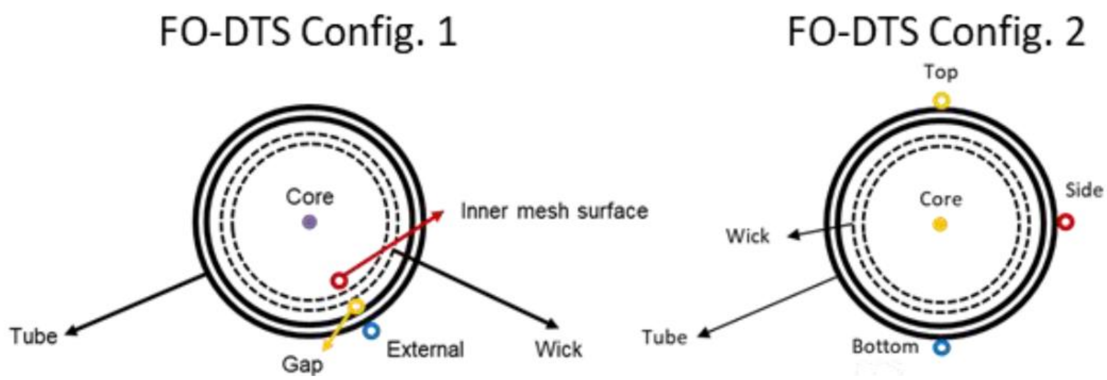

Figure 25. Fiber-optic distributed temperature sensor configurations utilized in the experiments [43].

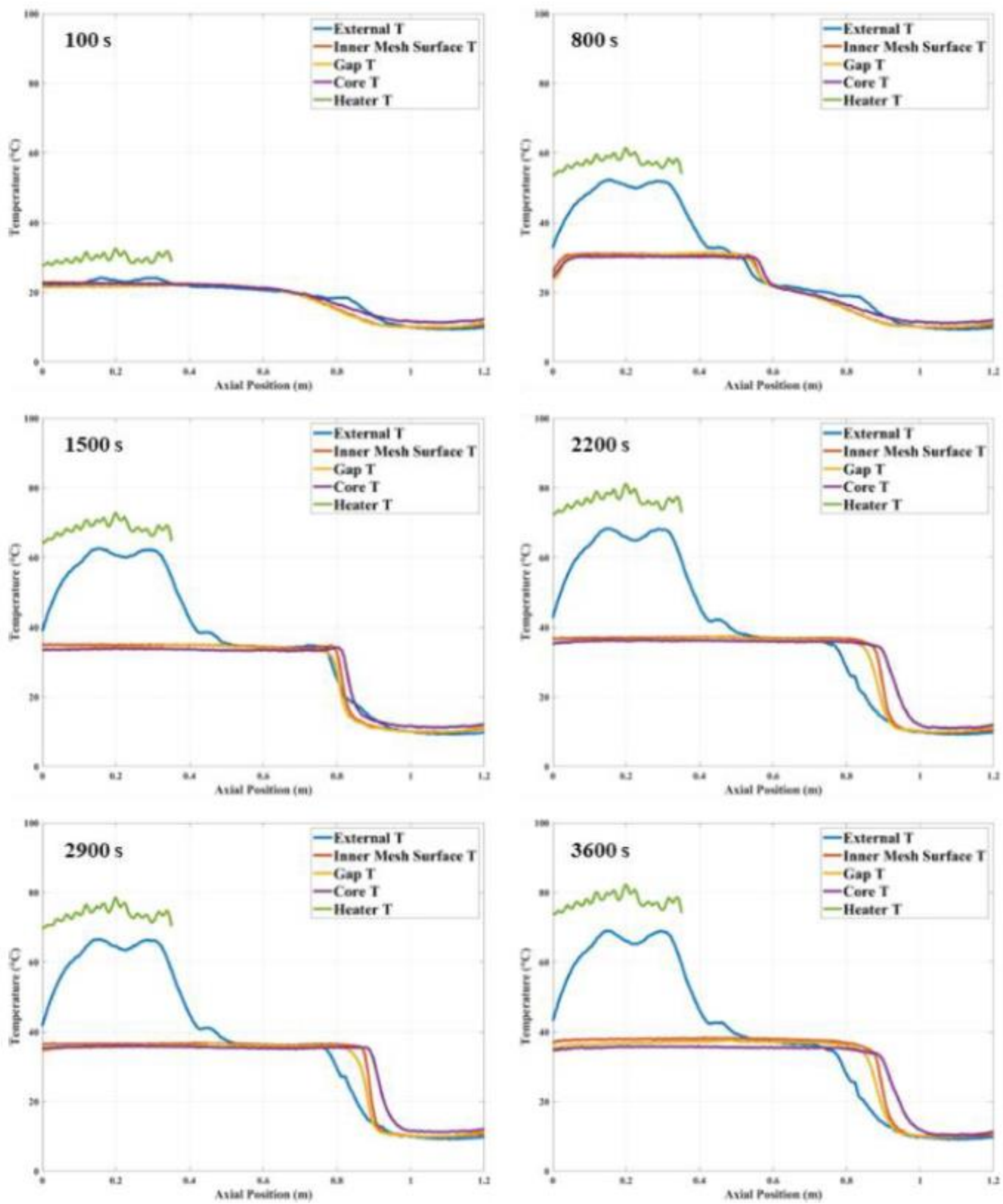

Figure 26. Axial temperature profiles for 25 W input power 10°C condenser coolant temperature [43].

4.5 Michigan Sodium Heat Pipe Facility (MISOH)

4.5.1 Facility Description

Researchers at the UM supported by DOE Nuclear Energy University Programs (NEUP) and the U.S. Nuclear Regulatory Commission (NRC) research grants designed and constructed two test facilities—MISOH-1 [95, 109-114] and MISOH-2 [96, 113]. These facilities are complementary; MISOH-1 is a single heat pipe test facility designed for separate effect tests, while MISOH-2 is intended to investigate integral effects using a heat pipe assembly. Both facilities employ high-temperature heat pipes provided by external vendors. Figure 27 shows a schematic of MISOH-1 that illustrates the structures of the evaporator, the adiabatic section, and the condenser. Heating is achieved through a silicon carbide radiative heater and cooling is facilitated by a multi-channel heat exchanger with internal fins. The heat exchanger functions as a gas-gap calorimeter using air as the coolant in the inner channel for high-temperature operation and ambient temperature water in the outer channel to reduce both the air temperature and the heat losses through the outer surface. Silicon carbide powder is applied in the gap to enhance conductive heat transfer efficiency. The actual cooling heat transfer rate is calculated using a sensible heat balance that considers both channels. Additionally, the adiabatic section includes heat-tracing between insulation layers to minimize thermal losses.

The instrumentation of the facility includes SCR and PID controllers, watt transducers, two Coriolis flow meters, 39 type-K TCs, and a data acquisition system. The silicon carbide heater permits heat inputs ranging from 500–3,800 W, while heat transfer coefficients (HTCs) from 4–500 W/m^2-K can be achieved at the adjustable condenser heat exchanger. The test section's inclination angle relative to gravity can be adjusted from 0–90 degrees. Most notably, x-ray radiography can be conducted with MISOH-1 to visualize two-phase flow at the evaporator section of the heat pipe.

In addition, the MISOH-2 facility was designed to investigate an array of 10 heat pipes, thus enabling the study of accident scenarios, such as single or multiple heat pipe failures, cascading failures, and non-uniform boundary conditions. The layout of the heat pipe array is a scaled-version of the Design A core of the INL/LANL SPR [2], adapted for different heat pipe diameters [96, 113]. The facility utilizes 16 U-shaped molybdenum disilicide ($MoSi_2$) heating elements strategically positioned to simulate the hexagonal fuel elements of the prototype. Calcium silicate grid spacer plates are employed to position the heat pipes and heaters. It is important to note that MISOH-2 does not have a core block; instead, there is air between the heaters and heat pipes, meaning the primary heat input to the heat pipes is via radiation. Radiation heat loss from the heaters to the surroundings is mitigated by a stainless steel plate and fiber insulation. The condenser’s heat exchangers in MISOH-2, similar to MISOH-1, are gas-gap calorimeters using air and water as coolants. Each heat pipe in the array has its dedicated heat exchanger at the condenser end.

A schematic diagram of the test facility is depicted in Figure 28. Power is supplied to the radiative $MoSi_2$ heaters through direct current (DC) power supplies, each with a maximum capacity of approximately 10 kW. The power input to the heat tracing of the adiabatic section is monitored using a watt transducer. The flow rates of air and water at the condenser heat exchangers are accurately measured by Coriolis flowmeters and individual rotameters for each heat pipe condenser. Additionally, numerous type-K TCs are strategically placed throughout the heat pipes to monitor temperature variations.

A schematic of the test facility can be seen in Figure 28. The power is supplied to the radiative $MoSi_2$ heaters through a DC power supply with a maximum power of ~5 kW. The power input of the heat trace is measured via a watt transducer. Coriolis flowmeters and rotameters measure the flow rates of air and water at the condenser heat exchangers. Each heat pipe has a designated rotameter for flow rate measurements. Numerous type-K TCs are placed throughout the heat pipes.

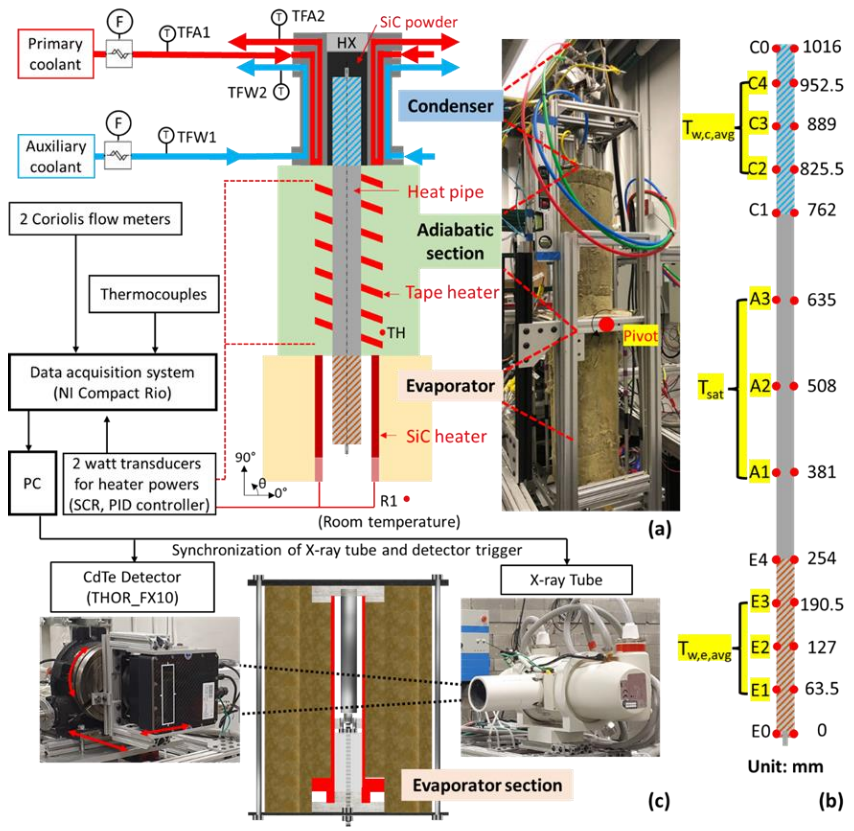

Figure 27. Schematic diagram of MISOH-1 showing detailed images of the heater and the condenser heat exchanger [111].

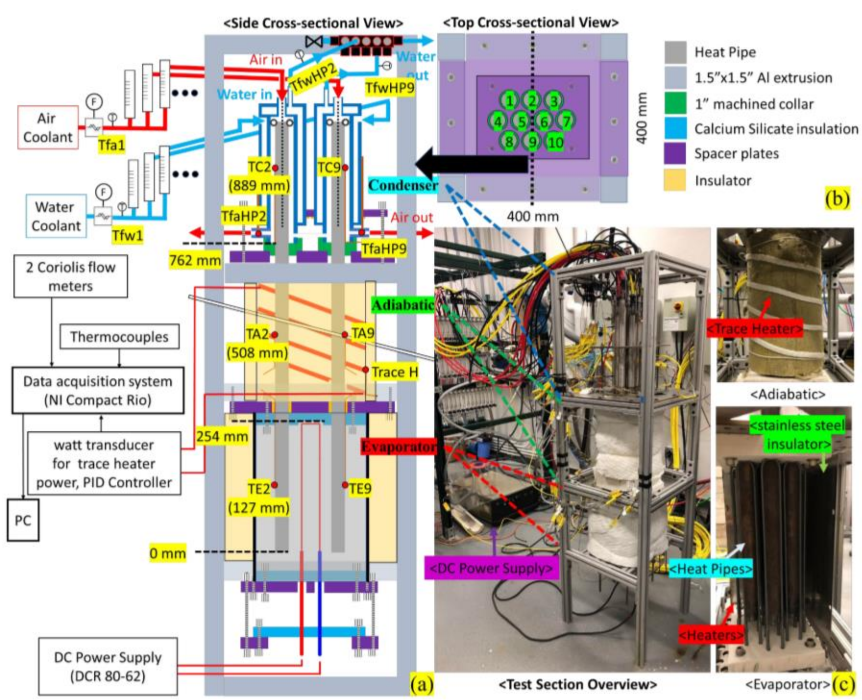

Figure 28. A description of MISOH-2 with (a) schematic diagram, (b) bundle layout, and (c) detailed images of the facility [96].

4.5.2 Results of MISOH-1 Experiments

In the separate effect tests [109-111], the start-up and steady-state performance of the single heat pipe were investigated under various operational parameters, such as heating and cooling boundary conditions and inclination angle. These tests involved three heat pipes with sodium-filling ratios of 67, 102, and 172%, respectively. Figure 29(a) illustrates the start-up process of a vertically-oriented heat pipe, highlighting three distinct vapor flow regimes based on the transition temperature, derived by Jang from the continuum flow criteria based on the Knudsen number ($Kn \leq 0.01$) and relations from the kinetic theory of gasses [115]. As the evaporator temperature exceeds the transition temperature, the transitional flow region, which combines free-molecular and continuum flow, is observed. Finally, when the entire heat pipe surpasses the transition temperature, it reaches the continuum flow regime, completing the start-up process. Figure 29(b) depicts the temperature evolution along the length of the heat pipe and its transition to an isothermal operational state.

The recently developed in-house high-speed x-ray radiography and image processing algorithms [116], specifically tailored for high-temperature objects, facilitate the capture of intricate details of the processes occurring within the heat pipe evaporator under various operational regimes. This advancement is demonstrated in Figure 30, which delineates the behavior of the sodium pool under different boiling regime. Importantly, the synchronization of radiography with temperature measurements not only significantly enhances data reliability but also proves to be instrumental in facilitating the validation of heat pipe codes.

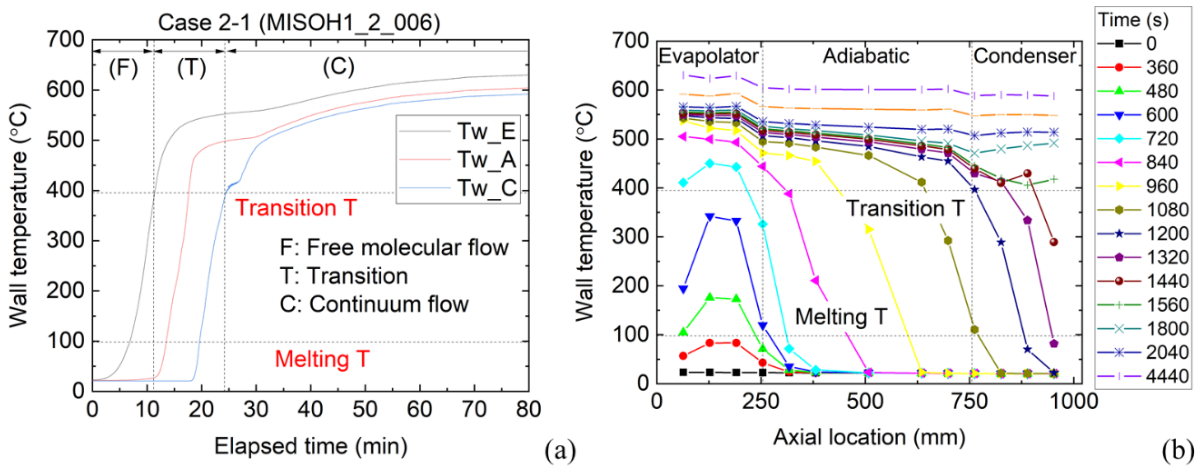

Figure 29. The start-up process and transition to isothermal operation state for a vertical heat pipe showing (a) wall temperatures over time, and (b) axial temperature profiles over time [93].

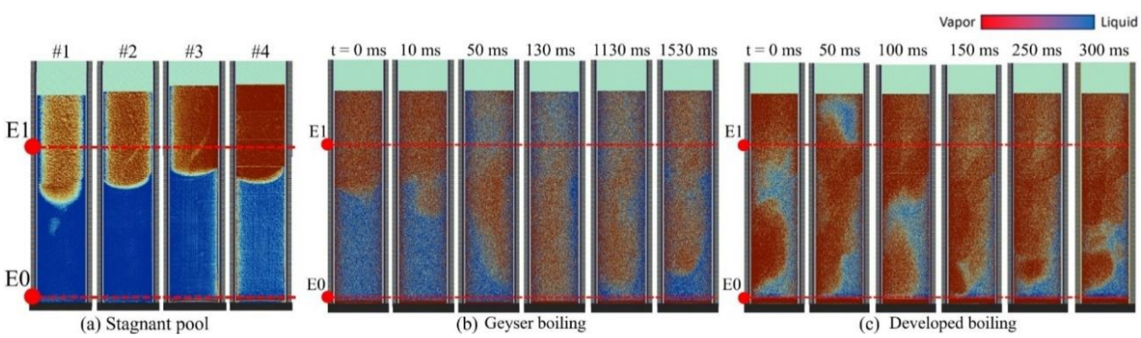

Figure 30. Visualization of sodium boiling phenomena in vertical heat pipe with 102% of sodium-filling ratio [111].

One of the significant findings in MISOH-1 was the identification and characterization of the geyser boiling regime in heat pipes with a large sodium filling ratio. This regime was investigated by Ahn et al. [95, 112] under various operation conditions. Thermocouple measurements taken during these transients were analyzed to determine the oscillations' period and amplitude, as depicted in Figure 31. Additionally, the study by Ahn et al. [95] reports an operating regime map that identifies periodic geyser boiling, intermittent geyser boiling, and developed pool boiling regions. A strong correlation was observed between the overall heat transfer rate and the oscillation period for periodic geyser boiling, with the period decreasing at higher heat transfer rates. The study further found that the oscillation amplitude is strongly influenced by the heat transfer rate in low cooling efficiency cases, leading to significant temperature surges under intermittent geyser boiling conditions. In addition to the geyser boiling, Huang et al. [114] introduced interesting phenomena observed in the operation of a sodium heat pipe under various conditions.

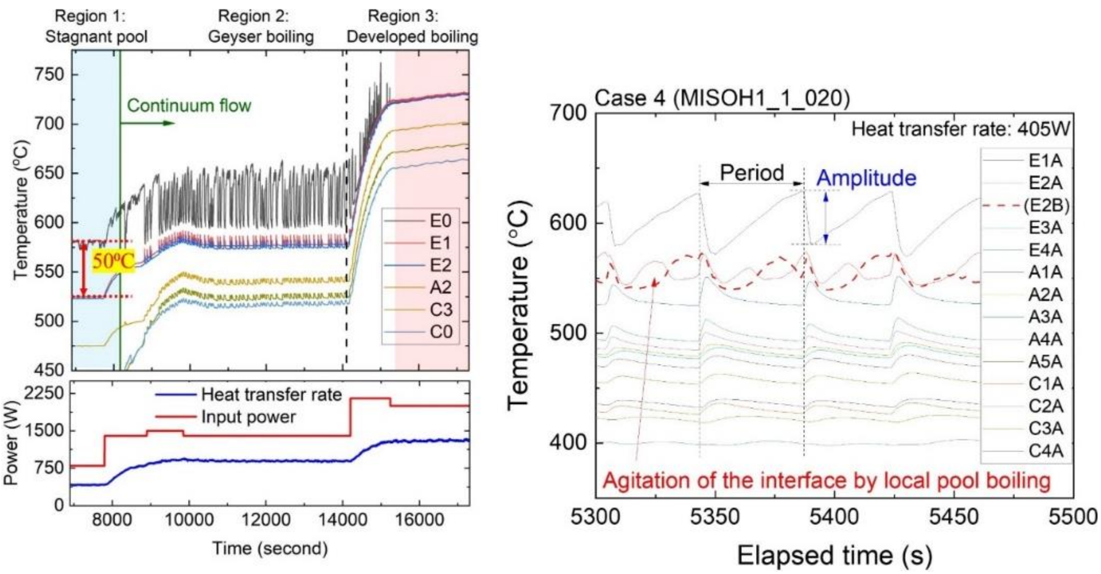

Figure 31. The observed periodic oscillations in temperature under the geyser boiling condition [95, 111].

4.5.3 Results of MISOH-2 Experiments

Data obtained from the MISOH-2 facility, which consists of an array of 10 heat pipes, include: (1) investigations of start-up under uniform and non-uniform heating and cooling conditions, (2) abrupt increases in the HTC at the condenser of a selected heat pipe within the array, and (3) simulations of single and double heat pipe failures. The temperature evolution of the MISOH-2 facility under uniform power heating and cooling conditions for both vertical and horizontal orientations is presented in Figure 32. The evaporator, adiabatic, and condenser temperatures of each of the 10 heat pipes are well above the transition temperature, confirming the successful start-up of the facility. This observation is consistent in both the vertical and horizontal orientations, suggesting the possibility of free-molecular flow in the condenser regions of multiple heat pipes. Additionally, the temperature response is noticeably quicker in a vertical orientation. The heating and cooling power plots reveal significant heat loss from the system.

In addition, a variety of tests were conducted to simulate different failure modes (single or multiple heat pipes at different locations). Heat pipe failure was replicated by replacing a heat pipe with a dummy tube of the same geometry. Additionally, the vertical and horizontal orientations were tested at various heating power levels (i.e., 3, 6.5, and 10 kW), using different arrangements of cooling and heating power condition. Detailed experimental results are available in the references [96, 113].

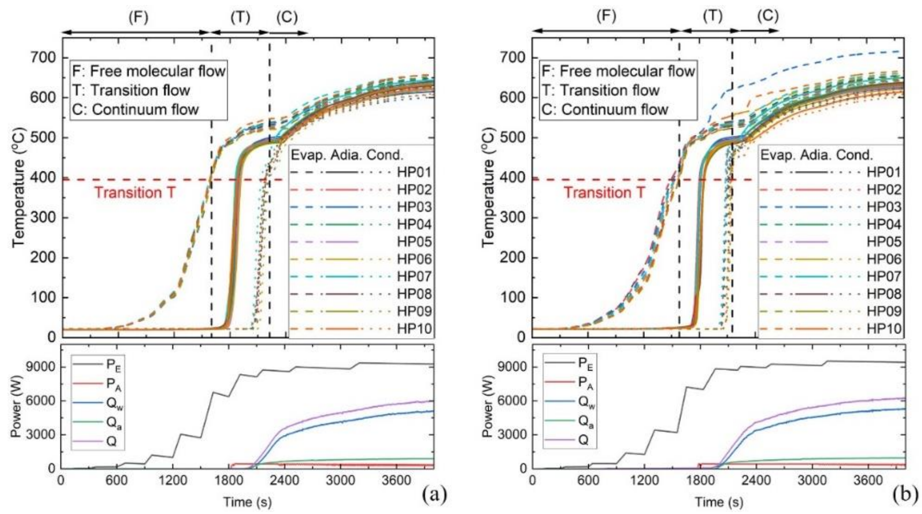

Figure 32. Start-up of the heat pipe array under uniform heating in (a) vertical and (b) horizontal orientations [113].

4.6 University of Wisconsin – Madison

4.6.1 Facility Description

The Thermal Hydraulics Laboratory at UW–Madison has developed comprehensive high-temperature heat pipe fabrication, testing, and advanced instrumentation capabilities. Their facilities house a 450 kV x-ray system, a laser welder, and a sodium loop with a cold trap, which is utilized to ensure the purity of the working fluid when filling heat pipes. They aim to address the knowledge gap on the x-ray imaging of the heat pipes, as well as to develop additional advanced measurement techniques, such as dual-energy radiography to observe wick dryout. A computer-aided drawing (CAD) section view of their experimental facility is shown in Figure 33, where heating is achieved by a Kanthal ribbon heating wire, while cooling is achieved via air or nitrogen flow through a cooling jacket. It should be noted the orientation of the heat pipe is adjustable from horizontal to vertical for both gravity-aided and counter-gravity operation (± 90°). An image of the facility under horizontal orientation can be seen in Figure 34, where the x-ray source and detector can be seen on opposite sides of the heat pipe.

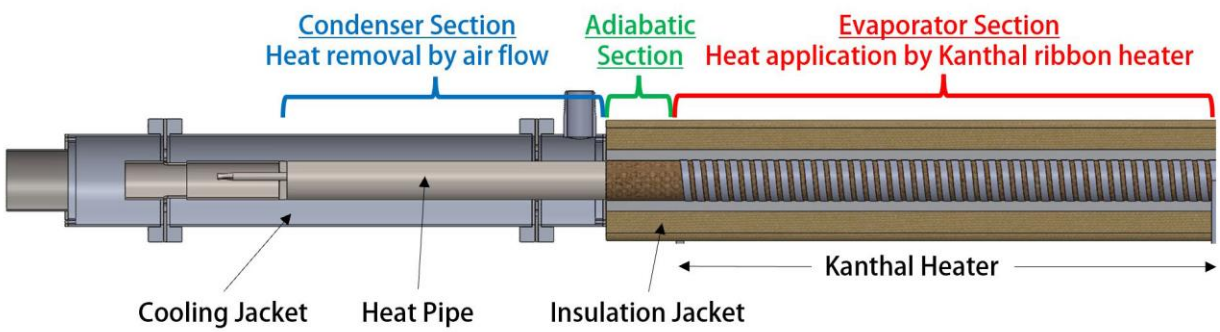

Figure 33. A CAD section view of the UW–Madison heat pipe test section [97].

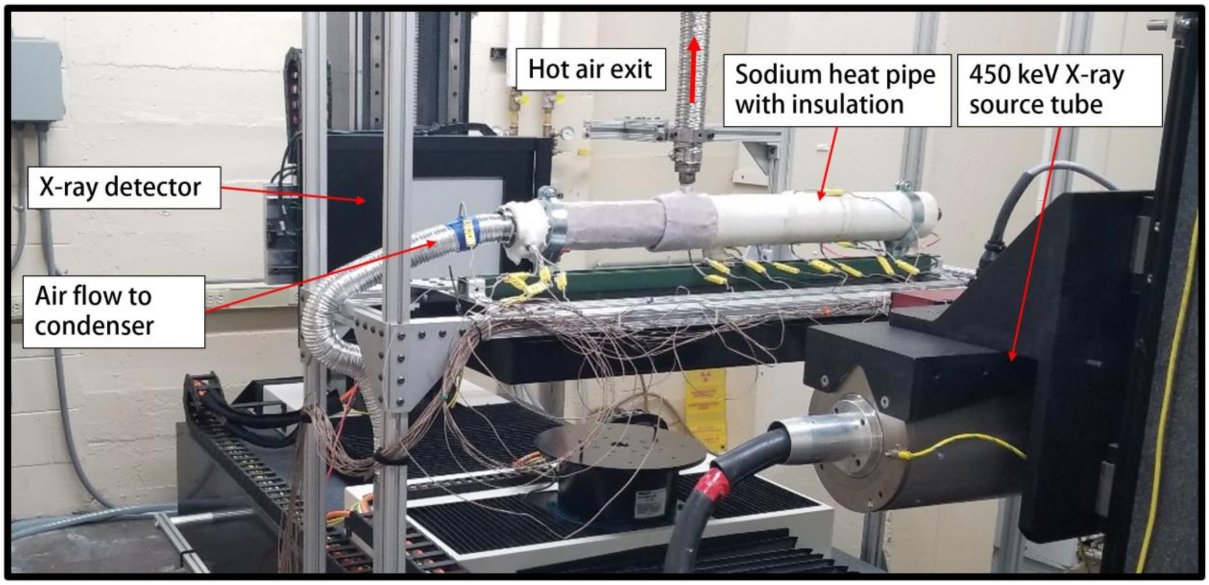

Figure 34. An image of the UW–Madison heat pipe facility under horizontal orientation [97].

4.6.2 Methods and Instrumentation

Tillman et al. recently demonstrated their x-ray tomography/fluoroscopy system with a sodium heat pipe and reported their procedures for heat pipe fabrication [97]. The manufacturing processes described by Edelstein and Haslett [117] were employed to fabricate, clean, fill, seal, and inspect a heat pipe with the design parameters shown in Table 9. The heat pipe dimensions and sodium charge were adapted from Teng et al. [118]. Most importantly, a schematic design of the heat pipe filling system can be seen in Figure 35, which uniquely utilized a 125 kV x-ray source to ensure highly accurate and controllable working fluid fill amounts. Once the heat pipe is filled, the working fluid is allowed to freeze before the application of high-vacuum to completely remove any non-condensable gasses present. The fill tubes are then crimped with a hydraulic tool and tungsten inert gas (TIG) welded for a permanent seal. After fabrication, the heat pipe is inspected by CT scanning with the 450 kV x-ray system to observe the wick and verify the volume of frozen working fluid.

Table 9. UW-Madison heat pipe design parameters [97].

Pipe outer diameter	1.25 in
Pipe inner diameter	1.12 in
Wick type	Crescent annular, 2 layers of #100 mesh
Wick ID	1.00 in
Annular gap	0.04 in
Pipe material	SS316
Evaporator length	18 in
Adiabatic section length	2 in
Condenser section length	10 in
Sodium fill amount	100 g

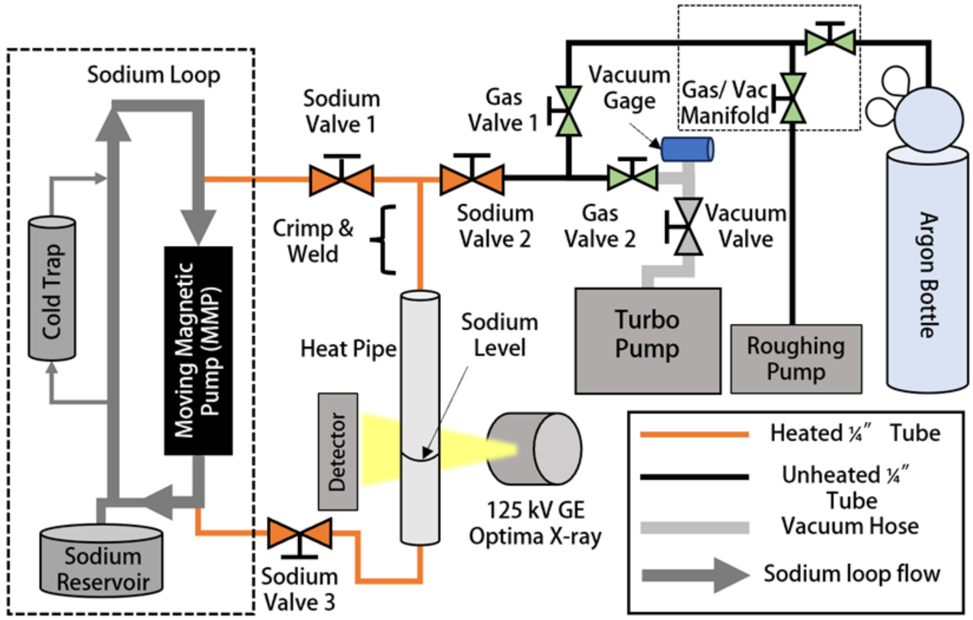

Figure 35. A schematic design of the heat pipe filling system utilizing a sodium loop with a cold trap [97].

X-ray imaging of the condenser region during initial tests clearly showed the progression of the liquid pool toward the condenser, as shown in Figure 3 [97]. Post-processing of the time series of x-ray images enables the evaluation of changes in the size of the liquid pool. Overall, UW–Madison's thermal hydraulics team have proved the effectiveness of their heat pipe manufacturing process and experimental techniques and have established future goals to incorporate additional instruments, such as FO-DTS sensors, to investigate phenomena including liquid sodium distribution in the wick, evaporator dryout, and heat pipe operational limits with high spatial and temporal resolution.

5. IRRADIATION OF HIGH-TEMPERATURE HEAT PIPES

Irradiation can alter or damage reactor materials through a variety of mechanisms, such as defect creation, embrittlement, swelling, irradiation creep, corrosion, and mechanical/thermal property changes. Current HPMR designs utilize heat pipes placed within or near the reactor core in order to transfer heat to the PCS [2, 8, 27]. This requires heat pipes to withstand continuous operation under high-temperatures and high-levels of gamma-ray and neutron irradiation. Therefore, irradiation effects on both thermal-hydraulic and mechanical properties of heat pipes must be quantified to assess operational efficiency and maintenance schedules. Furthermore, failure mechanisms or operational changes under irradiation should be identified for safety and reactor reliability.

Experience on the operation of high-temperature heat pipes under irradiation has been obtained indirectly through their use in the temperature control of irradiation capsules. These devices were designed to achieve relatively isothermal test specimen temperatures during irradiation testing of reactor structural and fuel materials in DOE laboratories [119, 120]. A schematic of a gas-gap dewar capsule is shown in Figure 36 [120]. Although the available data is limited and mostly qualitative, 29 irradiation capsules successfully demonstrated the operation of gas-loaded high-temperature heat pipes under reactor conditions for irradiation times averaging 6,000 hours and up to 23,000 hours [121]. The heat pipes were of various diameters and lengths and used sodium or potassium as working fluids. They employed screen wicks constructed using different screen sizes and number of layers, except for a unit that used a composite wick of screen and helical troughs [119]. The heat pipes were gravity-aided except for two cases. It should be noted that all heat pipes' walls and wicks were made of different types of stainless steel. Materials, working fluids, wick types, and dimensions of the heat pipes are shown in Table 10 as adapted from Ranken [121].

It should be noted that even though different heat pipe designs were employed, the overall design configuration of the heat pipes and the irradiation capsules were the same. Table 11 provides the testing parameters for the irradiation capsules. More detailed information on the heat pipes, irradiation capsules, and testing procedures can be found in Deverall et al. [119], Deverall and Watson [120], and Ranken [121].

The capsules utilized gas-loaded heat pipes to maintain the test specimens at a predetermined control temperature. The control temperature was set by modifying the amount of inert gas within the heat pipe and testing at a non-nuclear test bed with induction heaters and a gas-gap calorimeter, which can simulate reactor heating/cooling conditions [119]. This is critical for proper temperature control of the capsule since the nature of the facilities and capsule designs that were employed prevent the in operando measurement and control of testing conditions [120]. The temperature control abilities of heat pipes were validated in test beds before placement in the reactor.

The testing parameters during irradiation—including the pre-set temperature, maximum specimen temperature, nominal design power throughput, maximum power throughput, hours of operation, and maximum fluence—can be seen in Table 9. Maximum specimen temperatures reached during tests are available for the Hanford Engineering Development Laboratory (HEDL) cases and an ORNL case via thermal expansion temperature detectors [121]. Other methods, such as melt wires or silicon carbides, also were reported to be used to measure the maximum temperature attained during the experiments; however, none of these methods give temperature history information [119]. Maximum power throughput indicate the maximum power at which the heat pipes were tested and is available for all cases, except those tested in the Omega West Reactor (OWR). All testing was conducted at the Experimental Breeder Reactor II (EBR-II), except for the two OWR cases.

The adequate performance of the heat pipes under the tested conditions were determined based on post-irradiation examination (PIE). The methods employed were mainly qualitative and were based on heat pipe pressure and gas composition measurements, visual examination, x-ray examination, and testing at a non-nuclear test bed. It should be noted that x-ray examination and testing at a non-nuclear test bed were not applied to all heat pipes. The following assumptions were made when assessing heat pipe performance: (1) if the heat pipe's gas composition and pressure did not change post-test, it was assumed that the heat pipe operated near the pre-set temperature normally; (2) the occurrence of wick dryout during the test would cause visible discoloration or general damage to the capsule assembly; and (3) mechanical failures in the heat pipe casing causing working fluid loss would be visible during PIE. Testing at a non-nuclear test bed was conducted for the Naval Research Laboratory (NRL) heat pipes to ensure the proper operation and to reveal any malfunction or failure that may not be otherwise apparent.

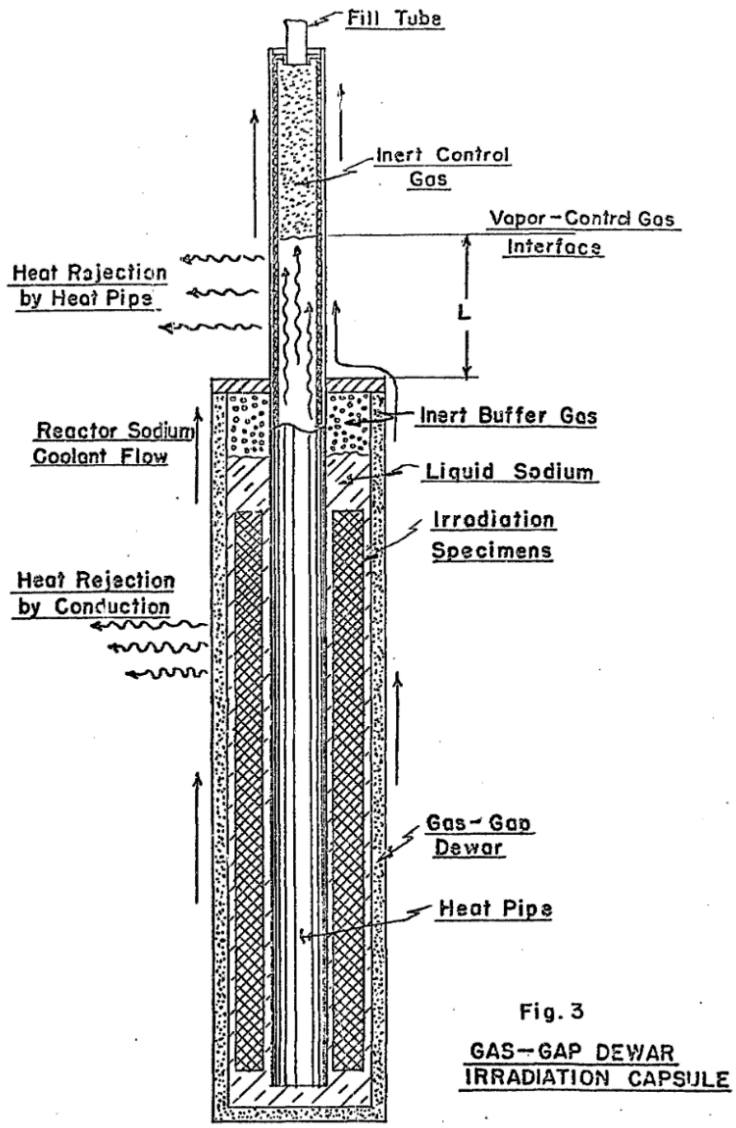

Figure 36. A schematic of a typical gas-gap dewar irradiation capsule [120].

The maximum specimen temperatures compared to the pre-set temperatures for the HEDL capsules are shown in Table 12, where significant differences in temperatures can be seen for some capsules. Ranken attributed these differences to the location of the temperature measurements within the specimen chamber, where the proximity to the reactor coolant can cause the specimens to run colder or hotter relative to the heat pipe [121]. It should also be noted that uncertainties during gas-loading to set the temperature, as well as instrument errors, can cause deviations between expected and observed values. Furthermore, Ranken also states that the maximum temperature measurements would greatly exceed the pre-set temperature in case the heat pipe fails, unlike what was observed in the data.

Overall, only a single failure was observed out of the 29 heat pipes used. This was an early failure of the weld in the OWR-2 test, which causes a sodium leak and was not related to long-term operation under irradiation [121]. However, it can be seen in Table 12 that the ORNL-C maximum specimen temperature exceeds the pre-set temperature by 100 K, which is attributed by Ranken as the combined effect of: (1) the generation of argon from the (n,p) reaction with potassium, and (2) the errors in the fill amount of inert gas and potassium working fluid [121]. Thus, this case was identified as a faulty operation and not a failure by Ranken.

Ranken identified the KA-II, NRL-6, HEDL-2, and HEDL-7 cases as particularly significant for the demonstration of long-term operation under irradiation. First, KA-II is reported to operate at 1,100 K for 6,400 hours without failure, which is a considerably high-temperature for stainless steel [121, 122]. Second, NRL-6 operated for 23,040 hours (2.63 years) with a total accumulated neutron fluence of 1 x 10^{23} n/cm^2 (E_n > 0.1 MeV) without any signs of failure. Finally, the HEDL-2 and HEDL-7 heat pipes operated against gravity successfully for 6,300 hours and 4,500 hours, respectively.

Through these findings, it can be concluded that stainless steel heat pipes with sodium or potassium working fluids can withstand long-term operation under high temperatures and fluences within the reactor cores. A majority of tests were conducted in the fast neutron spectrum of EBR-II with an accumulated operational experience of around 180,000 hours with operating temperatures ranging from 850–1,100 K. The main consequence of fast neutron irradiation was identified to be the transmutation of potassium into argon. However, this issue can be addressed by proper inert gas and working fluid fill amounts such that the operating pressure and temperature does not change significantly during operational life [121]. In addition, it was found that irradiation did not significantly increase corrosion rates. It should be noted that these findings are for austenitic stainless steel heat pipes with sodium and potassium working fluids, which is a common configuration in literature [2]. Yet, the findings did not reveal any failure mechanisms caused by irradiation, which might limit the life of alkali metal heat pipes [121].

Table 10. Design parameters of heat pipes used for the temperature control of irradiation capsules (* indicates gravity opposed operation) [121].

Test Series	Materials			Wick Type	Diameter (mm)		Length (mm)	
	Wall	Wick	Working Fluid		Outer	Vapor Core	Evap.	Cond.
OWR 1,2	347 SS	347 SS	Na	Screen (#160 Mesh)	12.7	9.5	140	65
K-1	304L SS	347 SS	Na	Screen (1 layer #60, 1 layer #100 mesh)	12.7	9.9	140	54
K-2, K-3a, K-4a	304L SS	347 SS	Na	Screen (3 layers #100 mesh)	12.7	9.8	250	65
K-3b	304L SS	347 SS	K	Screen (3 layers #100 mesh)	12.7	9.8	250	65
K-5	347 SS	347 SS	Na	Screen (6 layers #100 mesh)	28.0	24.1	406	114
KA I, II	304L SS	347 SS	Na	Screen (2 layers #250, 3 layers #100 mesh)	10.3	6.9	312	94
ORNL-A, -B	316 SS	304 SS	Na	Screen (3 layers #100 mesh)	12.7	9.4	228	127
ORNL-C	316 SS	304 SS	K	Screen (3 layers #100 mesh)	12.7	9.4	228	127
NRL 1-6	316 SS	316L SS	Na	Screen (2 layers #250, 6 layers #100 mesh)	22.2	16.9	380	160
HEDL 1,6	304L SS	304L SS	Na	Screen (1 layer #250, 3 layers #100 mesh)	18.6	15.3	144	110
HEDL 2,7*	304L SS	304L SS	Na	Screen (3 layers #250, 7 layers #100 mesh)	18.6	13.3	144	110
HEDL 3-5, 8-10	304L SS	304L SS	K	Screen/Trough (5 layers #250, 4 helical troughs 1.6 mm x 3.2 mm, 6 turns)	19.0	16.5	143	254

Table 11. Irradiation capsule heat pipe testing parameters (* indicates gravity opposed operation) [121].

Heat Pipe #	Test #	Pre-Set Temp. (K)	Design Power (kW)	Max. Power (kW)	Operation Time (h)	Max. Fluence (10^{22} n/cm^2) [E_n > 0.1 MeV]
OWR-1	OWR-1	1025	0.10		7,780	0.08
OWR-2	OWR-2	1025	0.10		4,850	0.059
K-1	X044	975	0.15	0.5	4,166	0.27
K-2	X092	1025	0.30	0.5	1,162	0.45
K-3a	X136	1025	0.30	0.5	2,431	0.61
K-3b	X136	875	0.30	0.5	2,431	0.58
K-4a	X136	1023	0.30	0.5	2,431	0.65
K-5	X171	1000	0.5	1.04	4,080	1.0
KA-I	X264	925	0.4	0.7	6,900	2.2
KA-II	X264b	1100	0.4	1.2	6,900	2.2
ORNL-A	X287	900	0.72	1.10	11,520	5.0
ORNL-B	X287	975	0.69	1.05	11,520	5.0
ORNL-C	X287	850	0.6	0.81	11,520	5.0
NRL-1	X200	920	2.5	4.5	6,250	3.3
NRL-2	X228	920	2.5	4.5	5,420	2.4
NRL-3	X255	920	2.5	4.5	11,904	7.0
NRL-4	X266	920	2.5	4.5	4,260	1.8
NRL-5	X284	920	2.5	4.5	13,440	5.0
NRL-6	X293	920	2.5	4.5	23,040	10.0
HEDL-1	AAIIB	923	1.5	3.0	6,300	4.5
HEDL-2	AAIIB*	1005	1.5	3.3	6,300	4.5
HEDL-3	B279	923	2.55	4.0	5,300	3.8
HEDL-4	B279A	913	2.55	4.0	4,500	3.2
HEDL-5	AAIIEE	1005	2.18	5.1	5,900	4.2
HEDL-6	X295	923	1.5	3.0	4,500	3.2
HEDL-7	X296*	1005	1.5	3.3	4,500	3.2
HEDL-8	B330	925	2.55	4.3	4,100	2.9
HEDL-9	B330A	923	2.55	4.3	4,800	3.4
HEDL-10		923	2.55	4.3	4,500	3.0

Table 12. Pre-set and maximum measured specimen temperatures for the HEDL capsules (* indicates gravity opposed operation) [121].

Heat Pipe #	Test #	Working Fluid	Pre-Set Temperature (K)	Max. Measured Specimen Chamber Temperatures (K)
ORNL-C	X287	K	850	950
HEDL-1	AAIIB	Na	923	935, 935, 875
HEDL-2	AAIIB*	Na	1005	1012, 1010
HEDL-3	B279	K	923	960, 951, 927, 953
HEDL-4	B279A	K	913	882, 886
HEDL-5	AAIIEE	K	1005	1010, 984, 936, 983
HEDL-6	X295	Na	923	967, 970
HEDL-7	X296*	Na	1005	975, 994, 1022
HEDL-8	B330	K	925	925, 927, 923
HEDL-9	B330A	K	923	923, 956, 947, 931

6. SOCKEYE VERIFICATION AND VALIDATION

Sockeye is an engineering-scale heat pipe design and simulation tool developed by the DOE Nuclear Energy Advanced Modeling and Simulation (NEAMS) program [31]. It is based on the Multiphysics Object Oriented Simulation Environment (MOOSE) framework, which enables its coupling to other MOOSE-based applications for the multiphysics simulations of reactor systems [102]. Sockeye V&V using experimental data is essential for its effective utilization in heat pipe analysis and HPMR development. Thus, to support and expedite HPMR development, the V&V of numerical tools, such as Sockeye, is one of the common objectives of the experimental efforts from different institutions described in the previous section. These experimental efforts should include a combination of separate and integral effect tests that can capture phenomena of different scales under a wide range of operating conditions for different heat pipe geometries and assemblies.

Requirements for the V&V of any numerical tool include the fidelity and abundance of experimental cases that can be used to benchmark simulation results. In the context of heat pipes, experimental data is particularly lacking for high-temperature heat pipes with geometries and materials applicable in HPMRs. In addition, the available experimental data is further limited by constraints on instrumentation caused by high-temperatures and the presence of liquid metals. Due to these difficulties related to high-temperature heat pipe experiments, the existing experimental data mainly reports external wall temperatures, which are relatively simple measurements, considering the complex two-phase flow that exist within the heat pipes.

The SAFE-30 heat pipe module test [123], work by Faghri et al. [69, 124], and the SPHERE tests [30], as well as DOE projects currently in progress, have previously been identified by Hansel et al. for use in Sockeye V&V activities [31]. Furthermore, Sockeye was recently benchmarked against data from the SAFE-30 heat pipe module test and SPHERE by Hansel et al. [30, 31, 125]. Reviewing the results of these benchmarking efforts is beneficial for a more complete understanding of how future experimental work may fit within the V&V efforts for Sockeye. It should be noted that analytical methods and test problems have also been utilized for Sockeye V&V; however, they were deemed outside the scope of the present report [125]. Furthermore, it should also be noted that Sockeye includes three different simulation options with varying capabilities and applications; these are the "two-phase flow model," "vapor only flow model," and the "conduction model" [126]. Different data sets or experimental requirements may be needed for the V&V of these different models.

Hansel et al. developed a test problem from the SAFE-30 heat pipe module experiments; however, the melting of the working fluid from room temperature was not considered since Sockeye's capabilities did not include frozen start-up at the time the work was conducted. The design parameters of the heat pipe employing a crescent annular wick was taken directly from the experimental work [123] except the wick permeability, which was not reported [31]. Reid et al. [123] computed the evaporator input power and radiative condenser cooling power. However, Hansel et al. modified these values by considering radiative heat losses in the condenser pool region and at the exposed surface of the evaporator. It should be noted that the "two-phase flow model" option was used for the simulations.

The simulation results yielded temperatures that are within the uncertainties of the experimental measurements for all five TCs placed at the axial locations of 0.216 m, 0.508 m, 0.711 m, 0.914 m, and 1.09 m, respectively. These temperature results compared to the experimental data for the simulated time interval that can be seen in Figure 37. It should be noted that the simulated time interval is significantly less than that of the experiment. This is due to the formation of a liquid pool at the condenser endcap causing numerical instabilities as the vapor void fraction approaches zero in the pool region. Other simulation results, such as steady-state temperature and pressure profiles, void fractions, and liquid/vapor velocities can be found in Hansel et al. [31].

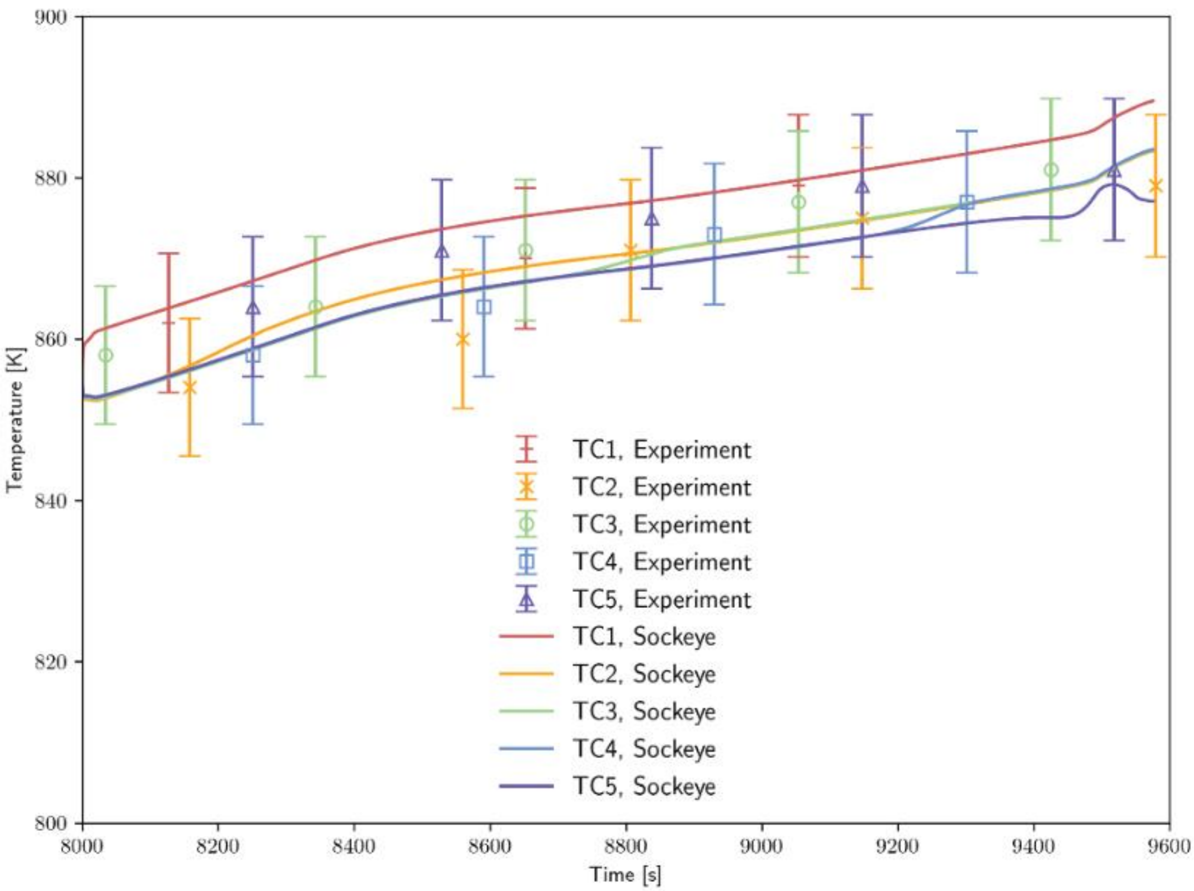

Figure 37. Validation of Sockeye temperatures with the SAFE-30 heat pipe module test [31].

In addition, data from the SPHERE facility was used for the validation of the "conduction model" option of Sockeye, which approximates the heat pipe as a superconducting material [125, 127, 128], since the treatment of non-condensable gasses was not implemented in the more rigorous "two-phase flow model" option [30]. The effects of non-condensable gasses were modeled based on the steady flat front model proposed by Marcus and Fleischman [129]. The experiments tested a gas-loaded heat pipe with an annulus-screen wick and a thermowell at the center of the vapor core. TCs were placed within the thermowell and on the outer wall of the heat pipe in order to obtain temperature data at various axial locations. The operational tests included frozen start-up, normal operation, and shut-down. The case used for V&V purposes involved the frozen start-up of the heat pipe from room temperature after which a constant power of 750 W was applied for 51.5 hours, followed by a cooling period of 39 hours with near-zero input power.

Simulation results showed good agreement with experiments at steady-state, except for an external wall TC, which was reported to be an erroneous measurement [30]. However, significant discrepancies were observed during shut-down, which was attributed to an inaccurate description of boundary conditions for cooling. This could be caused by inaccuracies in radiative cooling parameters such as emissivity, ambient temperature, and view factor. It should be noted that the "conduction model" includes many parameters that must be adjusted and/or tuned in order to replicate the experimental data. These parameters are either unknowns in the experiments, such as the mass of non-condensable gasses in the heat pipe and emissivities of the heat pipe wall and insulation, or they must be tuned since they are inputs to the model that must be determined empirically [30].

Overall, Sockeye V&V activities thus far reveal the importance of the characterization of the actual heating and cooling powers during experiments along with experimental factors, such as gap conductance. The SPHERE facility, as described in Section 4.2, includes upgrades such that these parameters can be estimated more accurately for simulation test problems. The efforts also emphasize the need for experiments utilizing: (1) more accurate and reliable measurement techniques, (2) advanced instrumentation for a more comprehensive experimental database, and (3) detailed records of experimental conditions and events. In particular, advanced instrumentation can enable the measurement of additional heat pipe parameters, minimizing estimations of certain parameters so that simulations may better reflect experimental conditions.

7. DISCUSSION

7.1 Summary of Recent Experiments

Recent experiments described in the present work demonstrate diverse and rigorous efforts aiding the maturation of heat pipe cooled microreactor technologies. Among them, KRUSTY is a crucial milestone on the path to microreactor development and deployment. However, it has highly specialized extra-terrestrial applications with an output of around 4 kWth, which is not currently at the scale of the proposed civilian applications. On the other hand, experiments supported by DOE through the national laboratory and university systems have focused on: (1) the development of test beds to generate data on the operation of heat pipes and heat pipe arrays, (2) the development of advanced measurement techniques for both high-temperature and low-temperature heat pipes, (3) the investigation of advanced manufacturing techniques, and (4) the performance enhancement of heat pipes and wicks.

As presented in detail in the previous section, all institutions are investigating advanced instruments, such as fiber-optic temperature sensing, x-ray radiography, and high-speed imaging. Breakthroughs in the utilization of such techniques are necessary to address the technical and regulatory challenges in the deployment of heat pipe microreactors. In addition, all institutions have identified the validation of numerical codes through high-spatial resolution data as a key purpose of their experimental facilities. Overall, it can be deduced that the research on heat pipe experiments in the U.S. focuses on the advancement of the understanding of heat pipe physics through advanced instrumentation, which will in turn translate into improved modeling techniques.

7.2 Proposed Future Directions

As heat pipe microreactors mature as a technology, it will become increasingly necessary to utilize advanced instrumentation for the detailed analysis of heat pipes. Presently, temperature, strain, and x-ray radiography techniques are the only available options for high-temperature heat pipe experiments. Some types of measurements that could be revolutionary in heat pipe experimentation may include:

- **Liquid/vapor mass flow rates:** Measurements of the mass flow rates, and/or the velocities for high-temperature heat pipes could be a giant leap in the field. These parameters can be utilized in numerous ways: (1) calculation of actual power throughput; (2) compressible flow analysis for vapor; (3) wick and interfacial stress calculations for entrainment; (4) characterization of the transient response of flow rate changes with evaporator power input, condenser cooling power, and limit conditions; (5) better identification of steady-state conditions, and (6) back-calculation of liquid/vapor flow areas. There is currently no robust method for measuring the liquid and vapor flow rates or velocities within a high-temperature heat pipe; however, methods such as laser spectroscopy were proposed [75].
- **Pressures and pressure drops:** It is challenging to effectively measure pressure within any type of heat pipe, but the difficulties are amplified with the presence of high-temperatures and liquid metals for heat pipes in microreactor applications. In addition, any pressure taps would not only be intrusive to the two-phase flow dynamics, but they would also present new safety risks since the heat pipe would seize to be a closed system. Another concern would be that the pressure tap might be exposed intermittently to liquid or vapor, which would affect how the data should be interpreted. Furthermore, the locations of the pressure taps must be carefully determined, and exactly what pressure is being measured should be conclusively shown. In particular, measurements of capillary pressure would be extremely valuable in assessing wick performance, and aiding wick development and modeling efforts. Last, effective measurements of liquid or vapor pressure drops would be very beneficial in pressure drop model validation.
- **Liquid, vapor, non-condensable, and vacuum fractions:** Knowing the mass or volume fractions of the liquid, vapor, non-condensable gasses, or vacuum within a heat pipe enable the direct calculation of additional parameters. One such parameter is interfacial heat flux, which can be used as an additional parameter to characterize transients when compared to the evaporator power input. Knowing the gas composition could also aid in the identification of corrosion and leakage within the heat pipe.

Besides the development of advanced instrumentation, another challenge HPMR developers face is on the regulatory front. The safe operation of the heat pipe and the heat pipe assemblies must be demonstrated via well-scaled experiments and validated modeling and simulation data for the licensing of a particular design. Literature is lacking in work related to the scaling of heat pipes using nuclear engineering scaling methodologies [79]. However, scaling analysis must be conducted and verified for the extension of the results from scaled-down facilities to prototypes. Scaling could be conducted on the heat pipe level [79] or on the system level. Besides the practical implications, development of robust scaling methods on the heat pipe level and the quantifications of scaling distortions would be a valuable tool in improving the understanding of heat pipe physics. Scaling analysis could focus on specific phenomena within a heat pipe, such as pressure drops, compressible flow dynamics, vapor diffusion during start-up, response to power transients, etc.

Finally, the reliability and predictability of heat pipes and heat pipe systems over the long-term need to be established, particularly to advance wick fabrication and heat pipe assembly methods [130]. These efforts could be supplemented by failure detection and prevention techniques, which could include autonomous approaches.

8. CONCLUSIONS

Microreactors are expected to satisfy the need for compact, carbon-free, off-grid power generation in numerous applications. In particular, heat pipe cooled microreactor designs provide unique advantages through passive core cooling, along with a more simple and compact design. Experiments supporting the R&D of heat pipe microreactors are needed to: (1) better understand heat pipe operation, particularly during transients and accident scenarios; (2) verify and validate models used in heat pipe and reactor design; (3) enhance heat pipe performance and reliability through novel wick designs or heat pipe fabrication techniques; and (4) to establish regulatory requirements for future deployment.

The present work provided a background on heat pipe experiments, briefly compiling and presenting different techniques and approaches. Subsequently, it identified phenomena of interest in heat pipes under various operating states in order to guide future experimental work and R&D efforts. Then, recent experimental work on heat pipes from leading institutions were presented and their different approaches, capabilities, and goals were discussed. In addition, legacy work on the operation of high-temperature heat pipes under reactor conditions were analyzed. Furthermore, V&V efforts for Sockeye were summarized and future experimental needs were identified. Finally, a discussion was given on the proposed directions for future experiments.

9. REFERENCES

1. Guillen, D.P., et al., *Development of a Non-Nuclear Microreactor Test Bed.* Transactions of the American Nuclear Society, 2019. **121**: p. 1623-1626.
2. Sterbentz, J.W., et al., *Preliminary Assessment of Two Alternative Core Design Concepts for the Special Purpose Reactor*. 2017, INL/EXT-17-43212, Idaho National Laboratory, Idaho Falls, ID.
3. Aumeier, S.E., et al., *Microreactor Applications in US Markets, Evaluation of State-Level Legal, Regulatory, Economic and Technology Implications.* 2023, INL/RPT-23-71733, Idaho National Laboratory, Idaho Falls, ID.
4. Abou Jaoude, A., et al., *An Economics-by-Design Approach Applied to a Heat Pipe Microreactor Concept.* 2021, INL/EXT-21-63067, Idaho National Laboratory, Idaho Falls, ID.
5. Testoni, R., A. Bersano, and S. Segantin, *Review of Nuclear Microreactors: Status, Potentialities and Challenges.* Progress in Nuclear Energy, 2021. **138**: p. 103822.
6. Guillen, D.P., *Review of Passive Heat Removal Strategies for Nuclear Microreactor Systems.* Nuclear Technology, 2023. **209**(sup1): p. S21-S40.
7. Faghri, A., *Heat Pipe Science and Technology*. 1995: Global Digital Press.
8. Poston, D.I., et al., *KRUSTY Reactor Design.* Nuclear Technology, 2020. **206**(sup1): p. S13-S30.
9. United States Nuclear Regulatory Commision. *Combined License Application Documents for Aurora – Oklo Power Plant Application*. 2022.
10. Lee, H., I. Mudawar, and M.M. Hasan, *Experimental and Theoretical Investigation of Annular Flow Condensation in Microgravity.* International Journal of Heat and Mass Transfer, 2013. **61**: p. 293-309.
11. Liao, Z. and A. Faghri, *Thermal Analysis of a Heat Pipe Solar Central Receiver for Concentrated Solar Power Tower.* Applied Thermal Engineering, 2016. **102**: p. 952-960.
12. Bienert, W.B., *The Heat Pipe and its Application to Solar Receivers.* Electric Power Systems Research, 1980. **3**(1-2): p. 111–123.
13. Vidal, C.R. and J. Cooper, *Heat-Pipe Oven: A New, Well-Defined Metal Vapor Device for Spectroscopic Measurements.* Journal of Applied Physics, 1969. **40**(8): p. 3370-3374.
14. Jung, E.G. and J.H. Boo, *Thermal Numerical Model of a High Temperature Heat Pipe Heat Exchanger Under Radiation.* Applied Energy, 2014. **135**: p. 586-596.
15. Yamawaki, S., et al., *Fundamental Heat Transfer Experiments of Heat Pipes for Turbine Cooling.* Journal of Engineering for Gas Turbines and Power, 1998. **120**(3): p. 580-587.
16. Yilgor, I., E. Lan, and S. Shi, *Design and Thermal-Hydraulic Performance Analysis of a Low-Temperature Heat Pipe Test Facility.* Nuclear Science and Engineering, 2023. **197**(5): p. 753-770.
17. Jackson, J.H. and P. Sabharwall, *Foreword: Special issue on the U.S. Department of Energy Microreactor Program.* Nuclear Technology, 2023. **209**(sup1): p. iii-v.
18. Lv, Q., et al., *Experimental Study of DRACS Thermal Performance in a Low-Temperature Test Facility.* Nuclear Technology, 2016. **196**(2): p. 319-337.
19. Sabharwall, P., et al., *Microreactor Program: Experimental Capabilities Summary.* 2021, INL/EXT-20-60441, Idaho National Laboratory, Idaho Falls, ID.
20. Sabharwall, P., et al., *Nonnuclear Experimental Capabilities to Support Design, Development, and Demonstration of Microreactors.* Nuclear Technology, 2023. **209**(sup1): p. S41-S59.
21. Sabharwall, P., et al., *SPHERE Assembly and Operation Demonstration.* 2020, INL/EXT-20-60782, Idaho National Laboratory, Idaho Falls, ID.
22. Kemme, J.E., *Heat Pipe Capability Experiments.* 1966, LA-3585, Los Alamos Scientific Laboratory of the University of California, Los Alamos, NM.
23. Cotter, T.P., et al., *Status Report on Theory and Experiments on Heat Pipes at Los Alamos.* 1965.
24. Woloshun, K., et al. *Boiling Limits in Heat Pipes with Annular Gap Wick Structures*. in *5th Joint Thermophysics and Heat Transfer Conference*. 1990.
25. Woloshun, K.A., M.A. Merrigan, and E.D. Best, *HTPIPE: A Steady-State Heat Pipe Analysis Program: A User's Manual.* 1988.

26. Cotter, T.P., *Theory of Heat Pipes.* 1965, LA-3246-MS, Los Alamos Scientific Laboratory of the University of California, Los Alamos, NM.
27. Levinsky, A., et al., *Westinghouse eVinci Reactor for Off-Grid Markets*, in *Transactions of the American Nuclear Society*. 2018. p. 931-934.
28. Swartz, M.M., et al. *Westinghouse eVinci™ Heat Pipe Micro Reactor Technology Development*. in *2021 28th International Conference on Nuclear Engineering*. 2021.
29. Wahlquist, S., et al., *A Critical Review of Heat Pipe Experiments in Nuclear Energy Applications.* Nuclear Science and Engineering, 2023. **197**(5): p. 719-752.
30. Hansel, J., et al. *Sockeye validation support using the SPHERE facility*. in *International Conference on Physics of Reactors 2022 (PHYSOR 2022)*. 2022.
31. Hansel, J.E., et al., *Sockeye: A One-Dimensional, Two-Phase, Compressible Flow Heat Pipe Application.* Nuclear Technology, 2021. **207**(7): p. 1096-1117.
32. Mueller, C. and P. Tsvetkov, *A Review of Heat-Pipe Modeling and Simulation Approaches in Nuclear Systems Design and Analysis.* Annals of Nuclear Energy, 2021. **160**: p. 108393.
33. Seo, J. and J.-Y. Lee, *Length Effect on Entrainment Limitation of Vertical Wickless Heat Pipe.* International Journal of Heat and Mass Transfer, 2016. **101**: p. 373-378.
34. Guichet, V., B. Delpech, and H. Jouhara, *Experimental investigation, CFD and theoretical modeling of two-phase heat transfer in a three-leg multi-channel heat pipe.* International Journal of Heat and Mass Transfer, 2023. **203**: p. 123813.
35. Tian, Z., et al., *Experimental evaluation on heat transfer limits of sodium heat pipe with screen mesh for nuclear reactor system.* Applied Thermal Engineering, 2022. **209**: p. 118296.
36. Wang, C., et al., *Experimental Study on Heat Transfer Limit of High Temperature Potassium Heat Pipe for Advanced Reactors.* Annals of Nuclear Energy, 2021. **151**: p. 107935.
37. Ma, Y., et al., *Experimental Study on Sodium Screen-Wick Heat Pipe Capillary Limit.* Applied Thermal Engineering, 2023. **227**: p. 120397.
38. Lee, D.H. and I.C. Bang, *Experimental Investigation of Heat Transfer Limitations in Concentric Annular Sodium Heat Pipes and Thermosyphon.* Applied Thermal Engineering, 2023. **232**: p. 121020.
39. Park, Y.Y. and I. Cheol Bang, *Experimental Study on 3D Printed Heat Pipes with Hybrid Screen–Groove Combined Capillary Wick Structure.* Applied Thermal Engineering, 2023: p. 121037.
40. Lee, D.H. and I.C. Bang, *Experimental investigation of thermal behavior of overfilled sodium heat pipe.* International Journal of Heat and Mass Transfer, 2023. **215**: p. 124449.
41. Tian, Z., et al., *Experimental investigation on the heat transfer performance of high-temperature potassium heat pipe for nuclear reactor.* Nuclear Engineering and Design, 2021. **378**: p. 111182.
42. Rudresha, S., E.R. Babu, and R. Thejaraju, *Experimental investigation and influence of filling ratio on heat transfer performance of a pulsating heat pipe.* Thermal Science and Engineering Progress, 2023. **38**: p. 101649.
43. Seo, J., H. Kim, and Y.A. Hassan, *Experimental study on the startup of the annular wick type heat pipe using fiber optical temperature measurement technique.* Physics of Fluids, 2023. **35**(5).
44. Dickinson, T.J., *Performance analysis of a liquid metal heat pipe space shuttle experiment*. 1996, Air Force Institute of Technology.
45. Ma, Y., et al., *Effect of Inclination Angle on the Startup of a Frozen Sodium Heat Pipe.* Applied Thermal Engineering, 2022. **201**: p. 117625.
46. Burban, G., et al., *Experimental investigation of a pulsating heat pipe for hybrid vehicle applications.* Applied Thermal Engineering, 2013. **50**(1): p. 94-103.
47. Yilgor, I. and S. Shi, *Experimental Investigation of Heat Pipe Flow Dynamics and Performance*, in *20th International Topical Meeting on Nuclear Reactor Thermal Hydraulics*. 2023, American Nuclear Society: Washington, DC.
48. Chen, J., et al., *Multiphase Flow and Heat Transfer Characteristics of an Extra-Long Gravity-Assisted Heat Pipe: An Experimental Study.* International Journal of Heat and Mass Transfer, 2021. **164**: p. 120564.

49. Sun, H., et al., *Experiment study on thermal behavior of a horizontal high-temperature heat pipe under motion conditions.* Annals of Nuclear Energy, 2022. **165**: p. 108760.
50. Dunn, P.D. and D. Reay, *Heat Pipes*. 4th ed. 1994, Tarrytown, NY: Elsevier.
51. Chi, S.W., *Heat Pipe Theory and Practice*. 1976: Hemisphere.
52. Seo, J., et al., *Design optimization of gap distance for the capillary limitation of a heat pipe with annular-type wick structure.* Physics of Fluids, 2022. **34**(6).
53. Seo, J., et al., *An experimental investigation on the characteristics of heat pipes with annular type composite wick structure.* Nuclear Engineering and Design, 2022. **390**: p. 111701.
54. Yilgor, I. and S. Shi, *Modeling and Investigation of Three Types of Wick Structures in Heat Pipe Microreactor Applications.* Transactions of the American Nuclear Society, 2021. **124**: p. 710-713.
55. Guillen, D.P., et al., *Additive Manufacturing of Heat Pipes for Microreactor Applications.* 2020, INL/CON-19-54498, Idaho National Laboratory, Idaho Falls, ID.
56. Jafari, D., W.W. Wits, and B.J. Geurts, *Metal 3D-printed wick structures for heat pipe application: Capillary performance analysis.* Applied Thermal Engineering, 2018. **143**: p. 403-414.
57. Yun, M., et al., *Design and Fabrication of Heat Pipes Using Additive Manufacturing for Thermal Management.* Applied Thermal Engineering, 2024. **236**: p. 121561.
58. Jafari, D., et al., *Pulsed mode selective laser melting of porous structures: Structural and thermophysical characterization.* Additive Manufacturing, 2020. **35**: p. 101263.
59. Jafari, D., W.W. Wits, and B.J. Geurts. *An investigation of porous structure characteristics of heat pipes made by additive manufacturing*. in *2017 23rd International Workshop on Thermal Investigations of ICs and Systems (THERMINIC)*. 2017.
60. Kim, D., *Experimental Investigation on the Characteristics of the Annular Type Composite Wick Heat Pipe*. 2022, Texas A&M University.
61. Dominguez Espinosa, F.A., T.B. Peters, and J.G. Brisson, *Effect of fabrication parameters on the thermophysical properties of sintered wicks for heat pipe applications.* International Journal of Heat and Mass Transfer, 2012. **55**(25): p. 7471-7486.
62. El-Genk, M.S. and H. Lianmin, *An experimental investigation of the transient response of a water heat pipe.* International Journal of Heat and Mass Transfer, 1993. **36**(15): p. 3823-3830.
63. Wang, J., *Experimental investigation of the transient thermal performance of a bent heat pipe with grooved surface.* Applied Energy, 2009. **86**(10): p. 2030-2037.
64. Bourdot Dutra, Carolina d.S., et al., *High-Fidelity Modeling and Experiments to Inform Safety Analysis Codes for Heat Pipe Microreactors.* Nuclear Technology, 2023: p. 1-25.
65. Deng, J., et al., *Experimental study on transient heat transfer performance of high temperature heat pipe under temperature feedback heating mode for micro nuclear reactor applications.* Applied Thermal Engineering, 2023. **230**: p. 120826.
66. Wang, C., et al., *Experimental Study on Transient Performance of Heat Pipe-Cooled Passive Residual Heat Removal System of a Molten Salt Reactor.* Progress in Nuclear Energy, 2020. **118**: p. 103113.
67. Chen, H.-X., et al., *Experimental study on frozen startup and heat transfer characteristics of a cesium heat pipe under horizontal state.* International Journal of Heat and Mass Transfer, 2022. **183**: p. 122105.
68. Tournier, J.-M. and M.S. El-Genk, *Startup of a horizontal lithium–molybdenum heat pipe from a frozen state.* International Journal of Heat and Mass Transfer, 2003. **46**(4): p. 671-685.
69. Faghri, A., M. Buchko, and Y. Cao, *A Study of High-Temperature Heat Pipes With Multiple Heat Sources and Sinks: Part I—Experimental Methodology and Frozen Startup Profiles.* Journal of Heat Transfer, 1991. **113**(4): p. 1003-1009.
70. Rosenfeld, J.H., et al., *An Overview of Long Duration Sodium Heat Pipe Tests.* AIP Conference Proceedings, 2004. **699**(1): p. 140-147.
71. Rosenfeld, J.H. and N.J. Gernert, *Life Test Results for Water Heat Pipes Operating at 200 °C to 300 °C.* AIP Conference Proceedings, 2008. **969**(1): p. 123-130.

72. Rosenfeld, J.H., et al., *Post-test analysis of a 10-year sodium heat pipe life test.* 2011, NASA/TM-2011-217206.
73. Anderson, W.G., P.M. Dussinger, and D. Sarraf, *High Temperature Water Heat Pipe Life Tests.* AIP Conference Proceedings, 2006. **813**(1): p. 100-107.
74. Martin, J.J. and R.S. Reid, *Life Test Approach for Refractory Metal/Sodium Heat Pipes.* AIP Conference Proceedings, 2006. **813**(1): p. 108-116.
75. Qin, S., et al., *Advanced Measurement and Visualization Techniques for High-Temperature Heat Pipe Experiments.* 2022, INL/EXT-22-68181, Idaho National Laboratory, Idaho Falls, ID.
76. Sellers, Z.D., et al., *SPHERE Gap Conductance Test.* 2022, INL/RPT-22-66992, Idaho National Laboratory
77. Hyer, H.C., D.C. Sweeney, and C.M. Petrie, *Functional fiber-optic sensors embedded in stainless steel components using ultrasonic additive manufacturing for distributed temperature and strain measurements.* Additive Manufacturing, 2022. **52**: p. 102681.
78. Thai, T.Q., et al., *Importance of Exposure Time on DIC Measurement Uncertainty at Extreme Temperatures.* Experimental Techniques, 2019. **43**(3): p. 261-271.
79. Yilgor, I. and S. Shi, *Scaling laws for two-phase flow and heat transfer in high-temperature heat pipes.* International Journal of Heat and Mass Transfer, 2022. **189**: p. 122688.
80. Shi, S., et al., *A Two-Phase Three-Field Modeling Framework for Heat Pipe application in nuclear reactors.* Annals of Nuclear Energy, 2022. **165**: p. 108770.
81. Button, M.C., *Devolopment of TDLAS Diagnostics for in situ Harsh Environment Water Vapor Temperature, Concentration, and Pressure Measurements*. 2019, The George Washington University.
82. Sockol, P.M., *Startup analysis for a high temperature gas loaded heat pipe.* 1973, NASA TM X-2840, Lewis Research Center, Cleaveland, OH.
83. Tournier, J.M. and M.S. El-Genk, *A vapor flow model for analysis of liquid-metal heat pipe startup from a frozen state.* International Journal of Heat and Mass Transfer, 1996. **39**(18): p. 3767-3780.
84. Cao, Y. and A. Faghri, *Closed-Form Analytical Solutions of High-Temperature Heat Pipe Startup and Frozen Startup Limitation.* Journal of Heat Transfer, 1992. **114**(4): p. 1028-1035.
85. Qin, S., et al., *Preliminary Design Needs for High-Temperature Heat Pipe Imaging System.* 2022, INL/RPT-22-70001, Idaho Falls, ID.
86. Stolte, K.N., et al., *Benchmark of the Kilowatt Reactor Using Stirling TechnologY (KRUSTY) Component Critical Configurations.* Nuclear Technology, 2022. **208**(4): p. 625-643.
87. McClure, P.R., et al., *Kilopower Project: The KRUSTY Fission Power Experiment and Potential Missions.* Nuclear Technology, 2020. **206**(1): p. S1-S12.
88. Gibson, M.A., et al., *The Kilopower Reactor Using Stirling TechnologY (KRUSTY) Nuclear Ground Test Results and Lessons Learned*, in *2018 International Energy Conversion Engineering Conference*. 2018.
89. Grove, T., et al., *Kilowatt Reactor Using Stirling TechnologY (KRUSTY) Cold Critical Measurements.* Nuclear Technology, 2020. **206**(1): p. S68-S77.
90. Sanchez, R., et al., *Kilowatt Reactor Using Stirling TechnologY (KRUSTY) Component-Critical Experiments.* Nuclear Technology, 2020. **206**(1): p. S56-S67.
91. McClure, P.R., et al., *KRUSTY Experiment: Reactivity Insertion Accident Analysis.* Nuclear Technology, 2020. **206**(1): p. S43-S55.
92. Poston, D.I., et al., *Results of the KRUSTY Nuclear System Test.* Nuclear Technology, 2020. **206**(1): p. S89-S117.
93. Poston, D.I., et al., *Results of the KRUSTY Warm Critical Experiments.* Nuclear Technology, 2020. **206**(1): p. S78-S88.
94. Du, H., I. Yilgor, and S. Shi, *Design of a Two-Phase Flow Facility for Investigation of Droplet Entrainment in Countercurrent Annular Flow.* Transactions of the American Nuclear Society, 2021. **125**(1): p. 1276-1279.

95. Ahn, T., et al., *Effects of Operational Conditions on the Geyser Boiling in the Sodium Heat Pipe for the Special Purpose Reactor*, in *Advances in Thermal Hydraulics*. 2022, American Nuclear Society: Anaheim, CA. p. 133-142.
96. Huang, P.-H., et al., *Experimental Study on the Start-up Characteristics and Performance of a Ten Sodium Heat Pipe Bundle Array*, in *20th International Topical Meeting on Nuclear Reactor Thermal Hydraulics*. 2023, American Nuclear Society: Washington, DC.
97. Tillman, E.M., G.F. Nellis, and M.H. Anderson, *X-ray Imaging of Flow Phenomena Within Sodium Heat Pipes for Microreactor Applications,* in *Transactions of the American Nuclear Society*. 2023: Indianapolis, IN. p. 904-907.
98. Foster, C., et al., *Impacts of Primary Heat Exchanger Design on Heat Pipe Microreactor Power Conversion,* in *Transactions of the American Nuclear Society*. 2023: Indianapolis, IN. p. 988-991.
99. Lee, K.-L., et al., *Titanium-Water Heat Pipe Radiators for Space Fission Power System Thermal Management.* Microgravity Science and Technology, 2020. **32**: p. 453–464.
100. Gibson, M.A., et al., *Heat Transport and Power Conversion of the Kilopower Reactor Test.* Nuclear Technology, 2020. **206**(1): p. 31-42.
101. Guillen, D.P. and D.S. Wendt, *Integration of a Microturbine Power Conversion Unit in MAGNET.* 2020, Idaho National Laboratory, Idaho Falls, ID.
102. Matthews, C., et al., *Coupled Multiphysics Simulations of Heat Pipe Microreactors Using DireWolf.* Nuclear Technology, 2021. **207**(7): p. 1142-1162.
103. Hyer, H., et al., *Performance of Microreactor Test Article with Embedded Sensors during Testing in the Single Primary Heat Extraction and Removal Emulator.* 2022, Oak Ridge National Laboratory, Oak Ridge, TN.
104. Holley, B.M. and A. Faghri. *Permeability and Effective Pore Radius Measurements for Heat Pipe and Fuel Cell Applications*. in *ASME 2004 International Mechanical Engineering Congress and Exposition*. 2004.
105. Byon, C. and S.J. Kim, *Capillary Performance of Bi-Porous Sintered Metal Wicks.* International Journal of Heat and Mass Transfer, 2012. **55**(15): p. 4096-4103.
106. Higuera, F.J., A. Medina, and A. Liñán, *Capillary rise of a liquid between two vertical plates making a small angle.* Physics of Fluids, 2008. **20**(10).
107. Bullard, J.W. and E.J. Garboczi, *Capillary rise between planar surfaces.* Physical Review E, 2009. **79**(1): p. 11604.
108. O'Brien, W.J., R.G. Craig, and F.A. Peyton, *Capillary penetration between dissimilar solids.* Journal of Colloid and Interface Science, 1968. **26**(4): p. 500-508.
109. Ahn, T., et al. *Experimental study on start-up characteristics of a sodium-filled heat pipe, using in-house high-resolution and high-speed radiation-based imaging system*. in *19th International Topical Meeting on Nuclear Reactor Thermal Hydraulics (NURETH-19)*. 2022.
110. Huang, P.-H., et al., *The Effect of Cooling Efficiency on the Startup Characteristic and Performance of the Sodium Heat Pipes for the Special Purpose Reactor with Different Filling Ratio*, in *Proceedings of Advances in Thermal Hydraulics*. 2022: Anaheim, CA. p. 120-132.
111. Huang, P.-H., et al., *Investigation of key parameters for the operation of a sodium heat pipe with visualization using X-ray radiography.* Applied Thermal Engineering, 2024, 121867.
112. Ahn, T., et al., *Geyser Boiling in a Sodium Heat Pipe.* 2024, (Unpublished Manuscript).
113. Huang, P.-H., et al., *Experimental Study of a Ten Sodium Heat Pipe Bundle Array with Various Failure Modes.* 2024, (Unpublished Manuscript).
114. Huang, P.-H., et al., *Evaporator Overheating and Dryout of a Sodium Heat Pipe with Visualization using X-Ray Radiography.* 2024, (Unpublished Manuscript).
115. Jang, J.H., *An analysis of startup from the frozen state and transient performance of heat pipes*. 1988: Georgia Institute of Technology.
116. Diaz, J., et al., *High-Resolution X-Ray Radiography Methods Developed for Post-CHF Experiment.* Nuclear Technology, 2023. **209**(10): p. 1442-1465.

117. Edelstein, F. and R. Haslett, *Heat Pipe Manufacturing Study.* 1974, NASA-CR-139140, National Aeronautics and Space Administration.
118. Teng, W., X. Wang, and Y. Zhu, *Experimental investigations on start-up and thermal performance of sodium heat pipe under swing conditions.* International Journal of Heat and Mass Transfer, 2020. **152**: p. 119505.
119. Deverall, J.E., et al., *Gravity-Assist Heat Pipes for Thermal Control Systems.* 1975, LA-5989-MS, Los Alamos, NM.
120. Deverall, J.E. and H.E. Watson, *Temperature Control of Irradiation Experiments with Gas-Controlled Heat Pipes*, in *Conference: International conference on irradiation experimentation in fast reactors*, . 1973: Jackson Hole, WY.
121. Ranken, W.A., *Irradiation of High Temperature Heat Pipes*, in *6th International Heat Pipe Conference*. 1987: Grenoble, France.
122. Şahin, S. and M. Übeyli, *A Review on the Potential Use of Austenitic Stainless Steels in Nuclear Fusion Reactors.* Journal of Fusion Energy, 2008. **27**(4): p. 271-277.
123. Reid, R.S., J.T. Sena, and A.L. Martinez, *Sodium heat pipe module test for the SAFE-30 reactor prototype.* AIP Conference Proceedings, 2001. **552**(1): p. 869-874.
124. Faghri, A., M. Buchko, and Y. Cao, *A Study of High-Temperature Heat Pipes With Multiple Heat Sources and Sinks: Part II—Analysis of Continuum Transient and Steady-State Experimental Data With Numerical Predictions.* Journal of Heat Transfer, 1991. **113**(4): p. 1010-1016.
125. Hansel, J.E. and L.C. Madeleine Charlot, *Increasing the Usability of Sockeye: Implementing Customer-Driven Modeling Improvements, Features, and Documentation of Sockeye.* 2021, INL/EXT-21-61673, Idaho National Laboratory, Idaho Falls, ID.
126. Hansel, J.E., *Heat Pipe Modeling Using Sockeye.* 2023, INL/MIS-23-73932, Idaho National Laboratory, Idaho Falls, ID.
127. Ma, M., et al., *A pure-conduction transient model for heat pipes via derivation of a pseudo wick thermal conductivity.* International Journal of Heat and Mass Transfer, 2020. **149**: p. 119122.
128. Panda, K.K., I.V. Dulera, and A. Basak, *Numerical simulation of high temperature sodium heat pipe for passive heat removal in nuclear reactors.* Nuclear Engineering and Design, 2017. **323**: p. 376-385.
129. Marcus, B.D. and G. Fleischman. *Steady-state and transient performance of hot reservoir gas-controlled heat pipes*. 1970. American Society of Mechanical Engineers.
130. Reid, R.S. and M.A. Merrigan, *Heat Pipe Activity in the Americas–1990 to 1995.* Los Alamos National Laboratory, Los Alamos, NM, 1997.